Membrane fission during bacterial spore development requires DNA-driven cellular inflation

Ane Landajuela[1,2†*], Martha Braun[2,3†*], Alejandro Martínez-Calvo[4], Christopher D. A. Rodrigues[5], Thierry Doan[6], David Z. Rudner[7], Ned S. Wingreen[8,9], Erdem Karatekin[1,2,3,10*]

1 Cellular and Molecular Physiology, Yale University, New Haven, CT, USA

2 Nanobiology Institute, Yale University, West Haven, CT, USA

3 Molecular Biophysics and Biochemistry, Yale University, New Haven, CT, USA

4 Grupo de Mecánica de Fluidos, Universidad Carlos III de Madrid, Spain

5 iThree Institute, University of Technology Sydney (UTS), Australia

6 Laboratoire d'Ingénierie des Systèmes Macromoléculaires, Aix-Marseille Université - CNRS UMR7255, Marseilles, France

7 Department of Microbiology, Harvard Medical School, Boston, Massachusetts,USA

8 Department of Molecular Biology, Princeton University, Princeton, NJ 08544, USA.

9 Lewis-Sigler Institute for Integrative Genomics, Princeton University, Princeton, NJ 08544, USA.

10 Université de Paris, SPPIN - Saints-Pères Paris Institute for the Neurosciences, Centre National de la Recherche Scientifique (CNRS), F-75006 Paris, France.

† These authors contributed equally

* To whom correspondence should be addressed

ane.landajuela@yale.edu

matha.braun@yale.edu

erdem.karatekin@yale.edu (lead contact)

SUMMARY

Bacteria require membrane fission for cell division and endospore formation. FisB catalyzes membrane fission during sporulation, but the molecular basis is unclear as it cannot remodel membranes by itself. Sporulation initiates with an asymmetric division that generates a large mother cell and a smaller forespore that contains only 1/4 of its complete genome. As the mother cell membranes engulf the forespore, a DNA translocase pumps the rest of the chromosome into the small forespore compartment, inflating it due to increased turgor. When the engulfing membranes undergo fission, the forespore is released into the mother cell cytoplasm. Here we show that forespore inflation and FisB accumulation are both required for efficient membrane fission. We suggest that high membrane tension in the engulfment membrane caused by forespore inflation drives FisB-catalyzed membrane fission. Collectively our data indicate that DNA-translocation has a previously unappreciated second function in energizing FisB-mediated membrane fission under energy-limited conditions.

HIGHLIGHTS

- Membrane fission during endospore formation requires rapid forespore inflation by ATP-driven DNA translocation.
- Forespore inflation increases the tension of the engulfment and forespore membranes to near lysis tensions.
- FisB catalyzes membrane fission, but only if the membrane tension is high.
- Membrane fission utilizes chemical energy transduced to mechanical energy during DNA-packing into the forespore.

INTRODUCTION

When nutrients are scarce, spore-forming bacteria initiate a morphological process called sporulation, which produces dormant, stress-resistant spores that can remain dormant for many years until conditions are favorable for germination (Moir and Cooper, 2015; Setlow, 2003). The first morphological event during sporulation is the formation of an asymmetric septum that produces a small forespore and a larger mother cell (Figure 1A). The mother cell membranes then engulf the forespore in a process reminiscent of phagocytosis. When the edges of the engulfing membrane reach the cell pole, they undergo membrane fission to release the forespore (Figure 1A inset), now surrounded by two membranes, into the mother-cell cytoplasm. The mother cell then packages the forespore in a protective cortex and coat while the forespore prepares for dormancy. When the forespore is mature, the mother cell lyses, releasing the dormant spore into the environment. Before asymmetric division, the chromosomes are remodeled into an axial filament with the origins of replication at the cell poles and the termini at the mid-cell (Webb et al., 1997). Thus, immediately after asymmetric division, only ~1/4 of the forespore chromosome is trapped inside the forespore (Wu and Errington, 1994, 1998). The rest of the chromosome is pumped into the forespore by an ATPase, SpoIIIE (Bath et al., 2000; Wu and Errington, 1997), consuming one ATP molecule per every two base pairs translocated (Liu et al., 2015). As the chromosome is packed into the forespore, the forespore volume doubles from its initial size of $\sim 0.1\ \mu m^3$ by the time the engulfment membrane migrates completely around the forespore and continues to grow to $\sim 0.3\ \mu m^3$ about 3 h after septation (Lopez-Garrido et al., 2018). Forespore inflation is driven by osmotic forces which are mainly due to the counterions that are needed to neutralize the highly charged DNA (Lopez-Garrido et al., 2018). Upon complete DNA packing, the pressure difference between the forespore and mother cell reaches ~60 kPa (Lopez-Garrido et al., 2018). It has been suggested that DNA translocation can be seen as an energy transduction process, converting the chemical energy stored in ~1.5 million ATP molecules to mechanical energy, stretching the thin peptidoglycan layer between the forespore and engulfment membranes and smoothing their wrinkles (Lopez-Garrido et al., 2018). However, it is not clear if this stored mechanical energy is ever utilized by the nutrient-deprived, sporulating bacteria, and if so, how.

Here, we investigate the relationship between forespore inflation driven by DNA translocation and the membrane fission event that releases the forespore into the mother cell cytoplasm. We previously showed that this event is catalyzed by the protein FisB that accumulates at the neck of the engulfing membranes during sporulation in *Bacillus subtilis* (Doan et al., 2013; Landajuela et al., 2021). FisB, a ~250 residue protein that is conserved among endospore-forming bacteria, is produced after asymmetric division in the mother cell (Doan et al., 2013). It possesses a short N-terminal cytoplasmic domain, a single-pass transmembrane domain (TMD), and a large extracytoplasmic domain (ECD, Figure 1B) (Landajuela et al., 2021). In cells lacking FisB (*ΔfisB*), engulfment proceeds normally, but the membrane fission step is impaired (Doan et al., 2013; Landajuela et al., 2021). Membrane fission can be assessed during a sporulation time course by labeling cells with a lipophilic dye that crosses the cell membrane inefficiently (Figure 1C). In cells that have not yet undergone fission, the dye has access to the forespore, engulfing, and mother cell membranes, resulting in a

stronger signal where these three membranes are in close proximity. By contrast, in cells that have undergone membrane fission, the dye only weakly labels the internal membranes, allowing the quantification of cells that have undergone fission at a given time point after initiation of sporulation (Landajuela et al., 2021) (Figure 1D). A functional GFP-FisB fusion forms dim mobile clusters (DMC), each containing ~12 GFP-FisB molecules. An intense spot at the engulfment pole (ISEP) containing ~40 copies of GFP-FisB appears around the time of membrane fission (Figure 1E,F and (Landajuela et al., 2021)). FisB localizes to the membrane neck that connects the engulfment membrane to the rest of the mother cell membrane based only on lipid-binding, self-aggregation, and the unique geometry encountered at the end of engulfment (Landajuela et al., 2021). FisB self-oligomerizes and binds acidic lipids, bridging artificial membranes, but does not appear to have other binding partners. During sporulation, the only location where FisB can bridge membranes is at the membrane neck that eventually undergoes membrane fission (Figure 1F), suggesting homo-oligomerization and trans interactions that bridge membranes are sufficient to explain FisB accumulation in the neck during late stages of engulfment (Landajuela et al., 2021). However, how membrane fission occurs at the last step of engulfment is not known.

Here we show that forespore inflation and FisB accumulation at the membrane neck are both required for efficient membrane fission. Interventions that slowed or prevented forespore area expansion delayed or inhibited membrane fission, even when FisB had accumulated at the membrane neck. Conversely, sporulating cells lacking FisB had impaired membrane fission but their forespores expanded. We suggest that high membrane tension in the engulfment membrane caused by forespore inflation drives membrane fission catalyzed by FisB. Our results demonstrate that part of the mechanical energy stored during the process of DNA packaging into the forespore is used for membrane fission.

RESULTS

FisB does not remodel membranes, but forms a stable, extended network on GUV membranes

The simplest mechanism of FisB-catalyzed membrane fission would involve direct membrane remodeling by FisB, similar to eukaryotic membrane fission machineries dynamin (Ferguson and De Camilli, 2012) or ESCRT-III (Schoneberg et al., 2017). To test this idea, we studied interactions of the FisB extracellular domain (ECD) with model GUV membranes. We fluorescently labeled recombinant purified FisB ECD with iFluor555-maleimide at a cysteine introduced at residue 123 (iFluor-FisB ECD, Figure 2A), a substitution that does not affect FisB's function (Landajuela et al., 2021). GUV membranes were labeled by including a fluorescent lipid in the lipid composition. Membranes and the labeled protein were then visualized using spinning-disc confocal (SDC) microscopy (Figure 2). We first incubated GUVs with various concentrations of iFluor-FisB ECD in a closed chamber for 60 min, then imaged the membranes and FisB ECD (Figure 2B). iFluor-FisB ECD did not bind GUVs lacking acidic lipids as reported previously (Landajuela et al., 2021). By contrast, iFluor-FisB ECD bound GUVs containing 30 mole % cardiolipin (CL). At 20 nM in solution FisB binding to GUVs was

136 barely detectable, but at ~75 nM, discrete FisB spots were visible. These spots were
137 diffused around the GUV membrane, reminiscent of the DMC in live cells. At 200 nM
138 and above, most GUVs were covered more uniformly and completely by iFluor-FisB
139 ECD. Consistent with previous work (Landajuela et al., 2021), and unlike many proteins
140 implicated in eukaryotic membrane fission (Campelo and Malhotra, 2012; Renard et al.,
141 2018; Simunovic et al., 2019), FisB did not cause any membrane deformations such as
142 tubulation or invaginations. Because such deformations are opposed by membrane
143 tension, we repeated these experiments using deflated GUVs with lower membrane
144 tension. Even at high coverage and when the GUVs were deflated, FisB did not cause
145 any remodeling of GUV membranes (Figure 2B). However, we noticed that deflated
146 GUVs covered with iFluor-FisB ECD did not display shape fluctuations typical of bare
147 deflated GUVs, suggesting FisB may form a fixed, extended network on the membranes
148 stabilizing the membrane shape.

149 We reasoned that if FisB ECD does indeed form an extended network on membranes,
150 its mobility should be low in such regions. To test this, we performed fluorescence
151 recovery after photobleaching (FRAP) experiments (Figure 2C). We incubated 1 μM
152 iFluor-FisB ECD with GUVs for 2 h. This allowed for a range of iFluor-FisB ECD
153 coverage of GUVs. Some GUVs were uniformly covered by iFluor-FisB ECD whereas
154 some others were covered only partially by iFluor-FisB ECD patches. We bleached the
155 iFluor-FisB ECD fluorescence in a rectangular region of interest (ROI) and monitored
156 the subsequent recovery on a given GUV. Recovery was faster for GUVs that had
157 partial, patchy iFluor-FisB ECD coverage, as new patches diffused into the bleached
158 region (Figure 2C upper row and Figure 2D). By contrast, there was virtually no
159 recovery for GUVs that were uniformly covered by iFluor-FisB ECD (Figure 2C lower
160 row and Figure 2D). To relate FisB ECD membrane coverage to mobility, we plotted the
161 mean iFluor-FisB ECD signal along the contour of the GUV, $F_{\mathrm{mean}}^{\mathrm{ECD}}$, against the fractional
162 fluorescence recovery 45 s after bleaching, as shown in Figure 2E. This analysis
163 showed that increasing FisB ECD coverage led to decreased FisB ECD mobility,
164 consistent with the idea that FisB ECD forms a denser, less dynamic network as
165 coverage increases.

166 To test how stable the FisB ECD network is, we dissolved the membranes after the
167 network had formed while observing iFluor-FisB ECD signals. Five to ten minutes after
168 addition of Triton X-100 the lipid signal disappeared, suggesting that the membranes
169 were dissolved. Remarkably, iFluor-FisB ECD signals were intact (Figure 2F), indicating
170 that once formed, the three-dimensional FisB ECD network was stable even after the
171 removal of the membrane.

172 Altogether, these data argue that FisB does not remodel membranes but is capable of
173 forming an extended, stable network in which individual FisB molecules are immobile.

174

175 **Forespore inflation accompanies membrane fission**

176 How can FisB catalyze membrane fission if it cannot remodel membranes by itself? We
177 reasoned that an additional cellular process should be involved, given that direct
178 interactions with other proteins could not be detected (Doan et al., 2013; Landajuela et
179 al., 2021). A process that could potentially influence membrane fission is the forespore

volume increase that occurs after asymmetric division due to translocation of DNA into the forespore by the ATPase SpoIIIE (Lopez-Garrido et al., 2018) (Figure 3A). However, whether and how this volume increase is related to membrane fission was not known. We began by investigating whether there was a correlation between forespore inflation and membrane fission. We used the lipophilic fluorescent dye 1-(4-trimethylammoniumphenyl)-6-phenyl-1,3,5-hexatriene p-toluenesulfonate (TMA-DPH) that allowed us to detect forespore contours of both cells that had undergone membrane fission and those that had not (Landajuela et al., 2021). We used a semi-automated active-contour fitting algorithm (Smith et al., 2010) and estimated the membrane areas from the surface of revolution around the long axis of symmetry (Methods). Three hours after initiation of sporulation via nutrient downshift, post-fission forespores were visually larger than their pre-fission counterparts (Figure 3B). Pre- and post-fission forespore areas decreased and increased as a function of time after the nutrient downshift, respectively (Figure 3C), suggesting cells with rapidly growing forespores underwent membrane fission, leaving behind smaller pre-fission forespores. Similar trends were obtained using a soluble CFP forespore marker (Figure S1), ruling out potential artifacts due to the use of a lipophilic membrane dye. The close link between forespore inflation and membrane fission was more evident when we plotted the percentage of cells having undergone membrane fission against the post-fission forespore area, which yielded a nearly linear relationship (Figure 3D).

The forespore area difference between pre- and post-fission cells, ΔA_{FS}, increased during sporulation to reach 1.3 ± 0.1 μm^2 (Figure 3E). Taking into account the 4 membrane leaflets that must grow together and assuming an area per lipid of $\sim 0.7\ \mathrm{nm}^2$, $\sim 7.4 \times 10^6$ new lipids must be added to the engulfment and forespore membranes during sporulation. Given that this growth occurs over ~2 h, lipids must be added at an average rate of ~1,000 lipids/s to the forespore and engulfment membranes. Interestingly, vegetative cell membrane areas grow at a comparable rate ($\dot{\mathrm{A}}_{\mathrm{veg}} = 0.020\ \mu\mathrm{m}^2/\mathrm{min}$, or about ~1000 lipids/s, taking into account two leaflets, 95% confidence interval: 0.007-0.023 μm^2/min, n=8 cells), consistent with the finding that phospholipid synthesis during sporulation occurs near the maximal rate associated with vegetative growth (Pedrido et al., 2013). Thus, forespore inflation requires high rates of *de novo* phospholipid synthesis despite energy-limiting conditions, and most of the newly synthesized lipids are utilized for forespore area growth during late stages of engulfment and after fission.

In summary, there is a clear correlation between membrane fission at the end of engulfment and forespore inflation, suggesting that forespore growth may facilitate membrane fission.

Hypothesis: increasing membrane tension during forespore inflation drives FisB-dependent membrane fission

How can forespore inflation promote FisB-mediated membrane fission? We hypothesized that increased membrane tension due to forespore inflation, coupled with FisB oligomerization at the membrane neck, could work synergistically to drive membrane fission. Because DNA pumping into the forespore leads to forespore inflation

through increased turgor and smooths membrane wrinkles (Lopez-Garrido et al., 2018), there must be an associated increase in the tension of the forespore membrane. Furthermore, because the forespore and engulfment membranes are separated through a thin layer of peptidoglycan only ~20 nm wide (Khanna et al., 2019; Tocheva et al., 2011), we expect the tension and the area of the engulfment membrane (which eventually undergoes fission) to increase together with that of the forespore membrane. The membrane tension of the forespore and engulfment membranes can be estimated from the excess osmotic pressure in the forespore, ~60 kPa (Lopez-Garrido et al., 2018). Assuming the two membranes that surround the forespore balance the excess osmotic pressure, then according to Laplace's Law $\Delta P = 4\gamma/R_{\mathrm{fs}}$, so that a forespore radius of $R_{\mathrm{fs}} = 400$ nm implies a membrane tension $\gamma \sim 6$ pN nm^{-1}. This is a very high value, around values expected for membrane rupture (Evans et al., 2003; Needham and Nunn, 1990; Ojkic et al., 2014). It is likely that the peptidoglycan cell wall surrounding the forespore may actually be necessary during forespore inflation to avoid membrane rupture (Lopez-Garrido et al., 2018).

The hypothesis that increasing membrane tension during forespore inflation drives FisB-dependent membrane fission leads to the following predictions. First, interfering with forespore inflation should hinder membrane fission. When forespore inflation is slowed or blocked, FisB should be properly localized to the membrane neck (provided engulfment is not compromised), because FisB's localization relies solely on its interactions with itself and with membranes, and the geometry of the neck (Landajuela et al., 2021). Second, in the absence of FisB, forespores should inflate but membrane fission should be impaired.

Blocking lipid synthesis impedes forespore inflation and membrane fission

Lipid synthesis is required during vegetative growth (Yao et al., 2012; Zhang and Rock, 2008) and sporulation (Pedrido et al., 2013; Schujman et al., 1998) and fatty acid availability determines average cell size (Vadia et al., 2017). When *B. subtilis* cells are placed in a nutrient poor medium, lipid synthesis is initially downregulated, but with the onset of sporulation, it returns close to the maximal rate (Pedrido et al., 2013). We reasoned that blocking lipid synthesis at different time points after the initiation of sporulation should block forespore area expansion at different stages. Furthermore, if forespore inflation is needed for membrane fission, the percentage of forespores blocked in inflation should correlate with those stalled at the pre-fission stage.

We blocked the synthesis of neutral lipids and phospholipids at different time points t after nutrient downshift using cerulenin, a drug that inhibits *de novo* fatty acid biosynthesis (Heath and Rock, 2004) (Figure S2A). We then probed the cells for membrane fission at $t = 3$ h using TMA-DPH labeling. We found that the earlier lipid synthesis was blocked, the smaller the fraction of cells that had undergone membrane fission at $t = 3$ h (Figure S2B,C). Both pre-and post-fission forespore membrane areas decreased with longer cerulenin application (Figure S2D). These results are consistent with previous reports that de novo lipid synthesis is needed for engulfment and forespore inflation (Lopez-Garrido et al., 2018; Pedrido et al., 2013). In addition to perturbing engulfment (Figure S2E,F) FisB accumulation at the fission site was reduced

268 in the presence of cerulenin (Figure S2G), making it difficult to infer the role of forespore
269 inflation in membrane fission. In order to unmask the contribution of forespore inflation
270 on membrane fission, we focused on cells in which FisB had successfully accumulated
271 at the membrane fission site. We discovered that an increasing fraction of these cells
272 failed to undergo membrane fission with longer cerulenin application (Figure S2H).
273 Thus, although impaired engulfment and FisB accumulation at the fission site partially
274 account for the membrane fission defects observed, blocking lipid synthesis inhibited
275 membrane fission even for cells with proper FisB localization, suggesting forespore
276 inflation facilitates membrane fission.

277

278 **Slowing DNA translocation slows membrane fission**

279 In addition to lipid synthesis, forespore inflation requires ATP-dependent DNA
280 translocation into the forespore. Accordingly, in a complementary set of experiments we
281 took advantage of previously characterized mutations in the DNA translocase SpoIIIE to
282 investigate whether forespore inflation contributes to membrane fission.

283 We began by using an ATPase mutant (SpoIIIE36) that is translocation defective
284 (Pogliano et al., 1997). In the absence of DNA pumping, the forespores remained small
285 and engulfment was severely perturbed (Figure S3A), similar to the engulfment
286 phenotype of the Δ*spoIIIE* mutant reported previously (Doan et al., 2013). Membrane
287 fission was severely impaired in these cells (Figure S3B) as was forespore area growth,
288 both for pre-fission and the small number of post-fission forespores (Figure S3C). The
289 fission defect can only be partly explained by deficient FisB localization, as 23±4 % of
290 the SpoIIIE36 cells had an ISEP at 3h after the nutrient downshift, compared to 70±6%
291 of WT cells (Figure S3G), yet only 5% of the SpoIIIE36 cells had undergone membrane
292 fission at this timepoint (Figure S3B). Importantly, among cells with an ISEP at the end
293 of engulfment, only ~16±4% of SpoIIIE36 cells had undergone membrane fission
294 compared to ~91±6% % of WT cells (Figure S3H). This difference was even more
295 pronounced when used a sensitized background in which FisB was expressed at ~8-
296 fold lower levels than wild-type (Doan et al., 2013; Landajuela et al., 2021). Under these
297 conditions, there were no post-fission SpoIIIE36 cells at hour 3 of sporulation among the
298 7% that had an ISEP. By contrast, 95% of the sporulating cells with SpoIIIE^{WT} that had
299 an ISEP had undergone membrane fission in this FisB low-expression background
300 (Figure S3G,H). Altogether, these results suggest that membrane fission requires both
301 FisB accumulation at the neck to be cut (ISEP formation) and forespore inflation.

302 The severe engulfment defects in the SpoIIIE36 mutant have the potential to obscure
303 the contribution of forespore inflation to FisB localization and membrane fission.
304 Accordingly, we took advantage of a second mutant (SpoIIIE^{D584A}) that translocates
305 DNA ~2.5-fold slower than wild-type (Burton et al., 2007) and does not have engulfment
306 defects (Figure 4). In sporulating cells expressing *spoIIIE*^{D584A}, forespore inflation was
307 delayed for post-fission cells and forespore area increased for pre-fission cells instead
308 of decreasing as for wild-type cells, suggesting slow forespore inflation slows
309 membrane fission (Figure 4A-C). This was more evident when the percentage of cells
310 that had undergone fission and post-fission forespore areas were plotted together as a

function of time (Figure 4D). The percentage of cells that underwent membrane fission increased with the increase in post-fission forespore area (Figure 4E). Importantly, engulfment (Figure 4F,G) and FisB localization (Figure 4H) were similar to wild-type. In fact, by hour 3 of sporulation, *spoIIIE*^{D584A} cells accumulated ~1.4-fold more FisB at the cell pole than did wild-type cells (Figure 4I), yet only ~40% of the *spoIIIE*^{D584A} cells had undergone membrane fission compared to ~75% of the wild type cells (Figure 4D), demonstrating that accumulating more FisB does not necessarily lead to more efficient membrane fission.

Together, these results strongly suggest that FisB accumulation at the membrane neck (ISEP formation) is *not* a sufficient condition for membrane fission; fission additionally requires forespore enlargement.

In the absence of FisB, forespores inflate but fission is impaired

Our data suggest that FisB accumulation at the fission site and forespore inflation work together to drive membrane fission. To investigate whether these two processes occur independently, we monitored forespore membrane area changes in cells expressing FisB at low levels or altogether lacking it.

We analzyed forespore area at different time points after a nutrient downshift, using TMA-DPH (Figure 5). As anticipated, most sporulating cells lacking FisB (*ΔfisB*) did not undergo membrane fission (Figure 1D) despite completing engulfment (Figure 5A) (Doan et al., 2013; Landajuela et al., 2021). Remarkably, the forespore areas of these pre-fission cells, $A_{\mathrm{FS}}^{\mathrm{pre}}$, increased as a function of time after the nutrient downshift, nearly doubling by $t = 3.5$ h, while those of wild-type cells decreased slightly during the same period (Figure 5B). The forespore areas of the small fraction of *ΔfisB* cells that underwent membrane fission (Figure 1), $A_{\mathrm{FS}}^{\mathrm{post}}$, were slightly larger than those of wild-type cells and followed a similar time course, increasing as a function of time (Figure 5C).

Sporulating cells expressing GFP-FisB at ~8-fold lower levels than wild-type undergo membrane fission more slowly (Figure S4). In these cells, post-fission forespore areas, A_{FS}^{post}, were slightly larger than those expressing GFP-FisB at native levels, and in both cases A_{FS}^{post} increased over time (Figure S4F). Similar to the Δ*fisB* mutant, the pre-fission forespore area increased as a function of time when GFP-FisB levels were reduced albeit the increase was more modest (Figure S4E).

Overall, these results indicate that forespore inflation occurs independently of FisB, but that forespore inflation is not sufficient to catalyze efficient membrane fission. When FisB is present, the fission process is greatly accelerated by forming an aggregate at the membrane neck to be severed, but only if the forespore is inflating (Figure 5D).

Modeling suggests increased engulfment membrane tension is the primary driver of FisB-catalyzed membrane fission

Next, we modeled the effect of increased membrane tension on membrane neck geometry, including the roles of hydrodynamic drag due the DNA pumping and the osmotic pressure difference between the cytoplasm and the lumen of the neck. We developed a minimal model based on free energy minimization, considering the free energy F of an axisymmetric and mirror symmetric membrane neck connecting two membrane sheets, corresponding to the local geometry of the neck connecting the forespore and mother cell membranes (see SI Appendix for details). The energy functional F consists of a term accounting for membrane bending and tension, F_{m}, another term, F_p, accounting for an osmotic pressure difference $\Delta p = p_{\mathrm{cyto}} - p_{\mathrm{peri}}$ between the cytoplasm and periplasm since the lumen of the neck is continuous with the periplasmic space, and finally a term representing any pulling force f on the forespore, e.g. due to DNA translocation, F_f.

We first explored the role of membrane tension, γ, on neck geometry. As shown previously (Landajuela et al., 2021) using a minimal model for the neck as a cylinder of radius r_{cyl} and length L_{cyl}, there are two regimes: (1) For a large neck (radius larger than a critical radius r_{crit}), membrane tension drives the neck to become ever larger. (2) For an initial $r_{\mathrm{cyl}} < r_{\mathrm{crit}}$, the neck will relax to a finite equilibrium radius set by the balance between membrane tension and membrane curvature. Intuitively, these two regimes follow because as the radius of the cylindrical neck grows, the area of the cylinder grows $\sim L_{\mathrm{cyl}}\, r_{\mathrm{cyl}}$, but the associated flat membrane areas on the mother cell and forespore *shrink* $\sim r_{\mathrm{cyl}}^2$. While the former term can dominate for small r_{cyl} leading to a local minimum, the latter term eventually dominates for large r_{cyl} implying the neck will open. The existence of a local minimum of neck radius is recapitulated by the full model in SI Appendix Eq. 1. As seen in SI Appendix Fig. 2, in regime (2) increasing membrane tension γ results in a narrowing of the equilibrium neck radius. While to our knowledge there has been no direct measurement of the membrane tension in *B. subtilis*, we find that reasonable values of $\gamma = 0.1 - 1$ pN nm^{-1} are sufficient to achieve a neck radius < 10 nm (Ojkic et al., 2014). It is likely that cell wall remodeling that drives engulfment (Ojkic et al., 2016) brings the neck radius into regime (2), because a neck forms and a small fraction of cells undergo membrane fission even in the absence of FisB (Figure 1 and Figure 5).

To examine the additional role of osmotic pressure difference between the cytoplasm and the lumen of the neck, we also minimized F at finite Δp. While $\Delta p = 0.1$ atm has little effect on the neck radius, $\Delta p = 1$ atm, which is realistic for *B. subtilis* (Lopez-Garrido et al., 2018; Ojkic et al., 2014) results in a substantial further reduction of the minimum neck radius (SI Appendix Fig. 2). This reduction makes sense, as higher osmotic pressure in the mother cell will tend to compress the volume of the periplasmic space contained within the neck.

By contrast, a pulling force on the forespore not only stretches the neck but also *increases* its equilibrium radius (see SI Appendix Fig. 4). A pulling force of $f = 50 - 100$ pN, around the maximum force that can be applied by one or two SpoIIIE motors translocating DNA into the forespore (Allemand and Maier, 2009; Liu et al., 2018), increases the minimum neck radius less than 1 nm when $\Delta p = 1$ atm, $\gamma > 5$ pN nm^{-1}.

One can understand this effect simply by considering the total force in the neck at the midpoint, which is the product of the circumference of the neck times the membrane tension, $f = 2\pi r_{\text{min}}\gamma$. So at fixed membrane tension γ, an increase of the pulling force f automatically implies an increasing r_{min}.

It is likely that the membrane tension in the rapidly expanding forespore and engulfment membranes is higher than in the mother cell membrane. We estimated an upper limit for this membrane tension gradient, by estimating the gradient that would be sufficient to drive a flux of lipids in the neck matching the observed average increase in forespore membrane area (see above and SI Appendix). Perhaps surprisingly, the resulting difference is only $\sim 10^{-7}$ pN nm^{-1}, which is orders of magnitude less than the expected overall membrane tension. Thus any flux of lipids between the mother cell and forespore will have negligible effect on the equilibrium results presented above. However, if this flux is impeded, e.g. by accumulation of FisB at the neck, the tension in the engulfment membrane around the forespore would increase further, possibly contributing to membrane fission (see below).

In summary, modeling suggests that the pulling force on the forespore exerted by DNA translocation has a negligible effect on neck geometry. By contrast, a realistically high membrane tension, possibly augmented by an osmotic pressure difference across the membrane, is sufficient to drive the equilibrium neck radius down to ≤ 5-10 nm, with two expected consequences. First, with a small neck radius, FisB can interact in *trans* and accumulate in the neck, facilitating membrane fission (Landajuela et al., 2021). Second, high membrane tension and a small neck radius likely both facilitate membrane fission.

Membrane fission due to high membrane tension

Our results so far suggest that increased membrane tension due to forespore inflation drives FisB-catalyzed membrane fission. Increased membrane tension in the engulfment membrane would provide a driving force for membrane flow from the mother cell to the engulfment membrane through the neck connecing the two compartments. One possibility is that by forming an oligomer at the membrane neck, FisB impedes lipid movement through the neck, further increasing the tension in the engulfment membrane, promoting membrane fission. Here we tested whether forespore inflation leads to membrane movement between the mother cell and engulfment membrane compartments.

We followed the kinetics of forespore area growth in individual cells and related the kinetics to membrane fission. Using time-lapse microscopy, we imaged individual sporulating cells labeled with the lipophilic dye FM4-64 (Lopez-Garrido et al., 2018) as shown in Figure 6A,B (see Figure S5 for more examples). While TMA-DPH crosses the cell membrane slowly, FM4-64 does not cross it, which allowed us to detect the time of membrane fission in addition to monitoring membrane areas. The non-fluorescent FM4-64 molecules in the aqueous phase exchange with the membrane-inserted fluorescent ones (Cochilla et al., 1999). Membrane fission isolates the small inter-membrane space from the bath, blocking exchange of bleached dyes with unbleached ones in the bath and accelerating decay of the florescence signals arising from the forespore and

engulfment membranes. A plot of forespore contour fluorescence as a function of time for individual cells shows a stable signal, which starts decreasing upon membrane fission. We cross-correlated these individual fluorescence profiles with a model decay function to determine the timing of membrane fission (Figure 6C). We defined t = 0 as the frame just preceding fission (Figure 6B,C) and aligned all measurements with respect to this time before averaging membrane areas as shown in Figure 6D,E. The rate of forespore area increase slowed gradually after membrane fission (Figure 6D). Remarkably, the mother cell area shrank before and grew after membrane fission (Figure 6E).

Until FisB accumulation at the membrane neck and membrane fission, there are two sources of lipids to support the growth of the forespore and engulfment membranes: de novo lipid synthesis and lipid flux between the mother cell and engulfment membranes (Figure 6F). After membrane fission, substantial expansion of the forespore and engulfment membranes can only be supported by de novo lipid synthesis. Thus, analysis of the rates of area changes can be informative about lipid flux through the neck. We focused on the mother cell area changes for this analysis, because the lipid synthesis rate in the forespore likely increases as a function of time as the lipid synthase genes are gradually translocated into the forespore (Pedrido et al., 2013). The mother cell area changed at rates of $-0.011\ \mu m^2/s$ (-262 lipids/s) and $+0.0032\ \mu m^2/s$ (+76 lipids/s) before and after fission, respectively. Assuming the rates of insertion into the mother cell of newly synthesized lipids pre- and post-fission do not change appreciably, we estimate ~340 lipids/s move through the neck toward the engulfment membrane before FisB accumulation –a significant fraction of the maximal cellular lipid synthesis capacity (see above).

Membranes lyse when stretched above only ~1 % in area (Evans et al., 2003). A deficit of ~300 lipids/s would cause a 1% deficit of the $\sim 2.5\ \mu m^2$ engulfment membrane area within a few minutes if the area expanded at fixed number of lipids. Thus, it is possible that FisB oligomerization interferes with lipid flux through the neck, leading to a further increase in the engulfment membrane tension, facilitating membrane fission.

DISCUSSION

Bacteria rely on membrane fission for every division cycle and during endospore formation. FisB is the only molecule described so far with a dedicated role in membrane fission in bacteria (Doan et al., 2013; Landajuela et al., 2021), but how FisB catalyzes membrane fission has remained unclear. Here we report that FisB does not remodel membranes directly but forms a stable network on them. Thus, another cellular process must be involved to achieve membrane fission at the end of engulfment. Surprisingly, we found that pumping of the chromosomal DNA into the forespore by the ATPase SpoIIIE –a seemingly unrelated process– is a necessary condition for FisB-dependent membrane fission. DNA pumping into the forespore leads to forespore inflation through increased turgor, stretching the thin layer of peptidoglycan between the forespore and engulfment membranes and smoothing membrane wrinkles (Lopez-Garrido et al.,

479 2018). FisB accumulation at the membrane fission site and forespore inflation are both
480 necessary conditions for efficient membrane fission.

481 We propose that increased membrane tension in the engulfment membrane due to
482 forespore inflation drives membrane fission (Figure 7). High membrane tension can
483 cause membrane fission through opening of a transient pore (Karatekin et al., 2003), as
484 was shown for fission catalysed by BAR domain proteins scaffolding a membrane tube
485 under extension (Simunovic et al., 2017). The presence of a protein scaffold on a
486 membrane tube has a dual role: slowing equilibration of membrane tension by impeding
487 membrane flow, and acting as a heterogeneous nucleation point for a membrane
488 defect, lowering the energy barrier for membrane poration (Simunovic et al., 2017).
489 Thus, FisB can similarly have a dual role in membrane fission. First, by oligomerizing at
490 the membrane neck, FisB impedes membrane flow from the mother cell membrane to
491 the engulfment membrane where tension is higher, leading to a further increase in
492 tension, making fission more likely. Second, the FisB oligomer-bare membrane interface
493 could provide a nucleation point for a membrane defect at high tension.

494 Membrane fission requires energy input. For all biological membrane fission reactions
495 described to date, membrane fission is energized and regulated locally. For the best
496 characterized cases, membrane fission proteins dynamin (Ferguson and De Camilli,
497 2012) or ESCRT III (Schoneberg et al., 2017) polymerize at the membrane fission site
498 and use the energy liberated by nucleoside triphosphate hydrolysis to reshape
499 membranes locally. By contrast, here we have found that membrane fission during
500 endospore formation in *B. subtilis* is energized indirectly through DNA translocation into
501 the forespore –a process that is required primarily for genetic inheritance and at first
502 sight bears little relation to the membrane fission that occurs at the opposite end of the
503 engulfment membrane. This situation is analogous to secondary transporters using
504 electrochemical gradients set by primary pumps such as the sodium-potassium ATPase
505 to energize secondary transport processes (Boron and Boulpaep, 2017).

506 Additionally, our results clarify the role of SpoIIIE in membrane fission during endospore
507 formation. It was originally proposed that in addition to DNA translocation, SpoIIIE
508 drives membrane fission because an ATPase deficient mutant resulted in membrane
509 fission defects (Liu et al., 2006; Sharp and Pogliano, 1999). However, SpoIIIE's role in
510 membrane fission remained unclear because the knock-out or ATPase dead mutants
511 (Figure S3 and (Doan et al., 2013)) cause severe engulfment defects. Since FisB
512 localization and membrane fission occur downstream of engulfment, any engulfment
513 defect would also produce FisB localization and membrane fission defects and would
514 not be particularly informative about membrane fission itself. Here we establish that
515 SpoIIIE does indeed play a critical role in membrane fission even in the absence of
516 engulfment defects, but this role is related to forespore inflation.

517 The membrane fission mechanism we have described here provides an elegant
518 example of how bacteria can use energy very efficiently under starvation conditions.
519 DNA translocation into the forespore is an energy-consuming process that cannot be
520 bypassed, but the byproduct of this process, namely increased turgor in the forespore,
521 can be harnessed to energize secondary processes. It will be interesting to see if

processes other than membrane fission are energized by mechanical energy stored in the inflated forespore.

ACKNOWLEDGEMENTS

We thank all members of the Karatekin laboratory for fruitful discussions and Jeorg Nikolaus (director of the Yale West Campus Imaging Core) for help with imaging. This work was supported by National Institute of General Medical Sciences and National Institute of Neurological Disorders and Stroke of the National Institutes of Health (NIH) under award numbers R01GM114513 and R01NS113236 (to EK). The content is solely the responsibility of the authors and does not necessarily represent the official views of the National Institutes of Health. We gratefully acknowledge a Yale University Predoctoral Fellowship to MB.

AUTHOR CONTRIBUTIONS

EK, MB, AL, and DZR conceived the study. MB carried out most of the experiments with purified proteins and artificial membranes, AL carried out live cell imaging and analysis. MB, EK wrote matlab scripts for image analysis, AL, MB analysed images. AMC+NSW developed the mathematical model, DZR, NSW and EK supervised the work. CDAR and TD provided reagents and intellectual input. EK wrote the manuscript, with input from all authors.

CONFLICT OF INTEREST

The authors declare they have no conflicts of interest.

FIGURE LEGENDS

Figure 1. FisB is required for efficient membrane fission during sporulation. **A.** Schematic of sporulation stages. Upon starvation, sporulation is initiated by asymmetric division into a mother cell (MC) and a forespore (FS). The MC then engulf the FS. At the end of engulfment, a thin neck or tube connects the engulfment membrane to the rest of the MC membrane (red box). Fission of the neck releases the FS, now surrounded by two membranes, into the MC cytoplasm. Upon maturation, the FS turns into a spore and the MC lyses to release it. Inset: membrane fission step marking the end of engulfment. **B**. Domain structure of FisB (Doan et al., 2013; Landajuela et al., 2021). **C**. Membrane fission assay. An aliquot of cells is labeled with the lipophilic dye 1-(4-trimethylammoniumphenyl)-6-phenyl-1,3,5-hexatriene p-toluenesulfonate (TMA-DPH) which fluoresces only once inserted into the membrane. The dye labels internal membranes poorly. If a cell has not yet undergone membrane fission at the time of TMA-DPH labeling, the dye has access to the space between the engulfment and FS membranes, resulting in brighter labeling of the MC, FS, and engulfment membranes when these are adjacent to one another (top row). After fission, the dye labels internal membranes poorly (bottom row). **D**. Time course of membrane fission for wild-type cells, *ΔfisB* cells, or *ΔfisB* cells complemented with mGFP-FisB expressed at native levels (strain BAM003). Some membrane fission occurs even in the absence of FisB (*ΔfisB*, gray markers). Mean±SEM from 3 independent experiments are shown (>300 cells were analyzed per point). **E.** Wide-field fluorescence microscopy images of cells expressing mGFP-FisB at native levels (strain BAM003). Aliquots were taken from the suspension at indicated times after nutrient downshift, labeled with TMA-DPH, and images of mGFP-FisB and membranes were acquired sequentially. Examples of sporulating cells with mGFP-FisB enriched at the septum (1.5 h), forming a dim mobile cluster (DMC; 2.5 h) and with a discrete mGFP-FisB focus at the cell pole (intense spot at engulfment pole, ISEP, 3 h) are highlighted with arrowheads. Scale bars represent 1μm. **F**. Schematic of FisB dynamics (Landajuela et al., 2021). At the end of engulfment, ~40 FisB molecules accumulate at the neck into an immobile cluster to catalyze membrane fission.

Figure 2. FisB does not remodel membranes. A. The soluble recombinant fragment of FisB comprising its extracytoplasmic domain (ECD) used in the experiments with GUVs. **B**. Interactions of FisB ECD with GUV membranes ("100% PC" and "30% CL" membranes are composed of (all mole %) 99 PC, 1 NBD-PE, and 30 *E. coli* CL, 69 eggPC, 1 NBD-PE, respectively). At low concentrations, FisB ECD forms small mobile clusters. With increasing concentration, labeling becomes more uniform. Even at high coverage or with deflated GUVs (right), no membrane remodeling is evident (deflated GUVs were composed of (all mole %) 25 *E. coli* PE, 5 *E. coli* CL, 50 *E. coli* PG, 19 eggPC and 1 DiD or NBD-PE (BS mix)). **C**. Mobility of FisB ECD decreases with increasing coverage. GUVs composed of BS mix were incubated with 1 μM iFluor555-FisB ECD for 2h. GUVs were covered with protein to varying degrees. Top row shows fluorescence recovery of a GUV with low iFluor555-FisB ECD coverage. Bottom row shows an example of a GUV fully covered with iFluor555-FisB ECD fluorescence that does not recover after photobleaching. Photobleached regions are indicated with boxes. **D**. Normalized fluorescence intensity from the boxed regions in C as a function of time.

591 **E**. Higher protein coverage (∝ mean GUV membrane intensity) leads to lower protein
592 mobility. The fractional fluorescence recovery 45 s post-bleaching ($(F_{45} - F_0)/(1 - F_0)$,
593 where F_{45} is the fluorescence intensity at 45 s and F_0 is the intensity just after bleaching,
594 both relative to pre-bleach intensity) is plotted as a function of mean GUV membrane
595 intensity. Each dot represents a GUV. **F**. FisB ECD forms a fixed, stable network on the
596 GUV membrane that persists even after the membranes are dissolved with detergent. 1
597 μM iFluor555-FisB ECD was incubated with deflated GUVs for 2h, then Triton X-100
598 was added (1.7 mM final concentration, 7-8-fold above the critical micelle concentration
599 (Tiller et al., 1984)), and the sample imaged 5-10 min thereafter.

600 **Figure 3. Forespore area increase during sporulation correlates with membrane**
601 **fission activity. A**. Schematic of SpoIIIE-mediated pumping of the chromosome into
602 the forespore leading to forespore inflation. **B**. Images show wild-type strain (PY79) at
603 *t*=3 h after nutrient downshift to initiate sporulation. Membranes were visualized using
604 TMA-DPH. Forespores of cells that have undergone membrane fission (red contours on
605 the right panel) are larger than those that have not yet undergone membrane fission
606 (blue contours). Scale bars represent 1 μm. **C**. Quantification of forespore membrane
607 area for cells that have (red, "post") or have not (blue, "pre") undergone membrane
608 fission. **D**. The percentage of cells that have undergone membrane fission as a function
609 of post-fission forespore area. **E**. The difference between post- and pre-fission
610 forespore areas, ΔA_{FS}, grows as a function of time. In C-E, mean±SEM of 3
611 independent experiments are shown, with 70 cells analyzed per data point.

612 **Figure 4. Slower forespore inflation leads to slower membrane fission with no**
613 **adverse effect on engulfment or FisB localization. A**. Fluorescence microscopy
614 images of TMA-DPH labeled wild-type SpoIIIE strain BAL039 (top row, times after
615 nutrient downshift are indicated). The lower row shows the same images, but with the
616 overlaid forespore contours for cells that have (red) or have not (blue) undergone
617 membrane fission. **B.** As in A, but for the slow DNA-pumping SpoIIIE strain BAL040
618 (SpoIIE^{D584A}). **C**. The average forespore area for pre- (blue) and post-fission (red) cells
619 as a function of time into sporulation for the SpoIIE^{D584A} (dashed lines, strain BAL040)
620 or wild-type (solid lines) cells (strain BAL039). (n=25-70 cells per data point). **D**. The
621 percentage of cells that have undergone membrane fission (left axis, black) followed a
622 very similar time course as the forespore area as a function of time (right axis, magenta)
623 for both WT (solid lines) and SpoIIE^{D584A} (dashed lines) cells. Both membrane fission
624 and forespore inflation were delayed in SpoIIE^{D584A} cells (>300 cells per data point). **E**.
625 The percentage of post-fission cells increased with increasing forespore area for both
626 WT (black) and SpoIIE^{D584A} (magenta) cells. WT data is copied from Figure 3 for
627 comparison. **F.** Fluorescence microscopy images of WT or SpoIIE^{D584A} cells expressing
628 mGFP-FisB at native levels in a *ΔfisB* background, probed 3h after the nutrient
629 downshift. Membranes were labeled with TMA-DPH. In cells expressing WT SpoIIIE
630 (top row) post-fission cells have larger forespores (red contours) and FisB is
631 accumulated at the membrane fission site (red arrowheads). At this stage, most cells
632 expressing SpoIIE^{D584A} are still in the pre-fission stage, even if engulfment is visually
633 complete and FisB has accumulated at the membrane fission site. **G.** Percentage of WT
634 or SpoIIE^{D584A} cells with engulfment membrane migration completed by t=3 h into
635 sporulation. Engulfment is not perturbed significantly by the slow DNA pumping by

SpoIIE^{D584A} (>300 cells per data point). **H**. FisB localization is not perturbed in SpoIIE^{D584A} cells compared to WT cells. **I**. Distributions of mGFP-FisB fluorescence intensities for the ISEP in willd-type ("WT") and the slow DNA pumping by SpoIIE^{D584A} mutant strain ("slow"). Representative regions of interest (and regions taken for background correction, "Bg") are shown on the example images on the left. The means ($\pm$ SD) are 70 ± 17 a.u. for WT and 99 ± 18 for SpoIIE^{D584A} ISEP intensities. Since for WT this intensity corresponds to ~40 copies of FisB (Landajuela et al., 2021), we conclude that nearly 60 copies are accumulated in SpoIIE^{D584A}. Scale bars represent 1 μm in A, B, and F. Means$\pm$SEM for 3 biological replicates are plotted in panels C-E, G,H. See Figure S3 for results with an ATPase dead SpoIIIE mutant.

Figure 5. **In the absence of FisB, forespores inflate but fission is impaired. A**. Representative images of wild-type (PY79) or *ΔfisB* cells (BDR1083) at the indicated times after nutrient downshift. Membranes were visualized with TMA-DPH. Lower panels show the FS contours for cells that have (red) or have not (blue) undergone fission. Scale bars represent 1 μm. **B.** The average pre-fission forespore area, $A_{\mathrm{FS}}^{\mathrm{pre}}$, grows during sporulation for *ΔfisB* cells, while it decreases for the wild-type strain. **C**. The average post-fission forespore area, $A_{\mathrm{FS}}^{\mathrm{post}}$, increases faster for *ΔfisB* cells. **D.** Summary of results. FisB catalyzes membrane fission in rapidly growing forespores (top row, "WT rapid inflation"). Slowly inflating forespores are less likely to undergo membrane fission even in the presence of FisB (middle row, "WT slow inflation"). In the absence of FisB, forespores inflate, but fission is rare. See Figure S4 for results with a strain expressing FisB at reduced levels. In B, C, mean$\pm$SEM of 3 independent measurements are shown (70 cells per data point).

Figure 6. Membrane flows between membrane compartments before and after membrane fission. **A**. Schematic showing how the timing of membrane fission is detected in time-lapse movies of individual cells. The dye (depicted as a star) becomes highly fluorescent upon insertion into the membrane. The lipid-inserted and free dyes exchange continuously, minimizing bleaching in pre-fission cells. Upon fission, the free dye has no longer access to the inter-membrane space, leading to the onset of an intensity decay. **B.** An example of a single cell, labeled with FM4-64, followed as a function of time (see Figure S5 for more examples). Top row shows a montage of FM4-64 fluorescence images as a function of time. The middle and bottom rows show the detected forespore and mother cell contours respectively, using an active-contour fitting algorithm. The frame preceding fission is indicated in the image (τ_{fiss}). Bar,1 μm. **C**. Plot of the mean FS contour FM4-64 fluorescence (black) as a function of time for the individual cell in B, displaying a relatively stable signal and a sudden decay upon membrane fission. Cross-correlation of the fluorescence signal with a model decay function (blue) was applied to determine the timing of membrane fission τ_{fiss}. **D**. Average of forespore cell membrane surface area of wild-type sporangia as a function of time (n=25). Time axes for individual cells were aligned such that $\tau_{\mathrm{fiss}} = 0$ min. Error bars represent SEM. The dashed blue and red lines are linear fits to the pre- and fission periods, with slopes 10.6×10^{-3} and $7.9 \times 10^{-3}\ \mu\mathrm{m}^2/\mathrm{min}$. **E**. Similar to J, but for the mother cell areas. The dashed blue and red lines are linear fits to the pre- and fission periods, with slopes -10.5×10^{-3} and $+3.2 \times 10^{-3}\ \mu\mathrm{m}^2/\mathrm{min}$. **F**. Schematic showing

680 sources and sinks of lipids. Before fission, newly synhtesized lipids are inserted into the
681 mother cell and engulfment membranes from the mother cell cytoplasm at rates M and
682 S_c, respectively. Lipids synthesized within the forespore are inserted at rate S_f, which
683 likely increases as lipid synthase genes initially located in the mother cell cytopolasm
684 are translocated into the forespore (Pedrido et al., 2013). Lipid flux through the neck (at
685 rate N) is only possible before fission.

686 **Figure 7. Proposed model of how forespore inflation drives FisB-mediated**
687 **membrane fission**. **A**. DNA translocation by the ATPase SpoIIIE inflates the forespore,
688 stretching the thin peptidoglycan layer between two and smoothing membrane wrinkles
689 (Lopez-Garrido et al., 2018). Increased membrane tension in the engulfment membrane
690 drives lipid flux through the neck between the engulfment and mother cell membranes,
691 partially supplying lipids needed for forespore inflation. **B**. FisB oligomerizes at the
692 membrane neck, impeding membrane flow and causing the engulfment membrane to
693 stretch further. **C**. Increased membrane tension drives membrane scission.

STAR★Methods

Key Resources Table

REAGENT or RESOURCE	SOURCE	IDENTIFIER
Chemicals, Peptides, and Recombinant Proteins		
TMA-DPH	Thermo Fisher Scientific	Cat#T204
FM4-64	Thermo Fisher Scientific	Cat#T13320
iFluor™ 555 maleimide	AAT Bioquest	Cat#1063
Cerulenin	Cayman Chemical	Cat# 10005647
Lipids	Avanti Polar Lipids	See Table S1 for a complete list of lipids used in this paper.
Experimental Models: Organisms/Strains		
Bacillus subtilis PY79		Tax. ID:1415167
See Table S2 for a complete list of strains used in this paper, including all the *Bacillus subtilis* PY79 variants	N/A	N/A
Recombinant DNA		
See Table S3 for a complete list of plasmids used in this paper. See Table S4 for a detailed explanation of their construction.	N/A	N/A
Oligonucleotides		
See Table S5 oligonucleotides	N/A	N/A
Software and Algorithms		
JFilament	(Smith et al., 2010)	http://athena.physics.lehigh.edu/jfilament/
SporeSize	This work	
Matlab	The MathWorks, Inc., Natick, MA	https://www.mathworks.com/

697

698 **Contact for Reagent and Resource Sharing**

699 Further information and requests for resources and reagents should be directed to and
700 will be fulfilled by the Lead Contact, Erdem Karatekin (erdem.karatekin@yale.edu)

701

702 Method details

703 Experimental Procedures

704 General *B. subtilis* methods

705 *B. subtilis* strains were derived from the prototrophic strain PY79 (Youngman et al.,
706 1983). Sporulation was induced in liquid medium at 37°C by resuspension according to
707 the method of Sterlini-Mandelstam (Sterlini and Mandelstam, 1969). *B. subtilis* strains
708 were constructed using plasmidic or genomic DNA and a 1-step competence method.
709 Site directed mutagenesis was performed using Agilent's Quick-change Lightning kit
710 following manufacturer's instructions and mutations were confirmed by sequencing.
711 Tables of strains (Table S2) and plasmids (Table S3) can be found in Supplemental
712 Information.

713 Fluorescence microscopy from batch cultures

714 500 µl samples at indicated times during sporulation were taken and concentrated ~50-
715 fold by centrifugation (3300xg for 30 s). Membranes were stained with 1-(4-
716 trimethylammoniumphenyl)-6-phenyl-1,3,5-hexatriene *p*-toluenesulfonate (TMA-DPH;
717 Molecular Probes) at a final concentration of 100 µM and the cells were then
718 immobilized on a 2% agarose pad made with sporulation buffer covered with a no.1.5
719 coverslip, after which the cells were immediately imaged live. In most cases
720 fluorescence microscopy was performed using a Nikon Ti microscope equipped with a
721 ×100 Plan Apo 1.45 NA phase-contrast oil objective, an Orca-Flash4.0 V2 CMOS
722 camera (Hamamatsu Photonics, Shizuoka,Japan) and a Spectra X light engine
723 (Lumencor, Beaverton, OR, USA), all controlled by Nikon Elements software (Nikon
724 Corp. Tokyo, Japan). Excitation of TMA-DPH was achieved using the 395/25 nm band
725 of the SpectraX system and Chroma's ET 49000 single band filter set the DAPI filter set.
726 (λ_{ex}=395/25 nm; λ_{em}=431/28 nm). Excitation light intensity was set to 50% and exposure
727 times were 200 ms.

728 In experiments shown in **Figure *6*** and S3, cells were prepared following the same
729 procedure but visualized on a Leica DMi8 Wide-field Inverted Microscope equipped with
730 a HC PL APO 100× DIC objective (NA=1.40), and an Andor iXon Ultra 888 EMCCD
731 camera (Andor Technology Ltd., Belfast, Northern Ireland) and a Spectra X light engine
732 (Lumencor, OR,USA) controlled by the LAS X program (Leica Microsystems, Wetzlar,
733 Germany). Excitation of TMA-DPH was achieved using the 395/25 nm band of the
734 Spectra X system and the Leica DAPI filter set (λ_{ex}=395/25 nm; λ_{em}=460/50 nm).
735 Excitation light intensity was set to 50% and exposure times were 300 ms. .

736 Images were processed using the ImageJ software. Contours generated using

737 JFilament were coloured using Photoshop.

738

739 **Time-lapse fluorescence microscopy**

740 Cells were visualized on a Leica DMi8 Wide-field Inverted Microscope equipped with a
741 HC PL APO 100× DIC objective (NA=1.40) and an iXon Ultra 888 EMCCD Camera from
742 Andor Technology. Sporulation was induced at 37°C. To visualize the membranes,
743 0.5 µg/ml FM4-64 was added to the culture ~1 hours after sporulation induction and
744 incubation continued for another hour. Then a 10 µl sample was taken and transferred
745 to an agarose pad prepared as described (Lopez-Garrido et al., 2018). Pictures were
746 taken in an environmental chamber at 37°C every 5 min for at least 2 hours. Excitation
747 of FM4-64 was achieved using the 575/25 nm band of the SpectraX system and a
748 custom FM4-64 filter set (λ_{ex}=395/25 nm; λ_{em}>610nm). Excitation light intensity was set
749 to 5% to minimize phototoxicity and exposure times were 100 ms. For presentation
750 purposes, sporangia were aligned vertically (with forespore on top) by rotating them
751 using ImageJ. Contours generated with JFilament were colored using Photoshop.

752

753 **Expression, purification, and labeling of recombinant proteins.**

754 FisB ECD and mutants were purified as described in (Landajuela et al., 2021). Briefly,
755 His_6-FisB ECD was expressed in *E. coli* BL21 (DE3) (New England Biolabs,
756 Ipswich,MA,USA) and purified using HisPur™ Ni-NTA Resin (Thermo-Fisher Scientific,
757 Waltham, MA, USA). Protein expression was induced with 1 mM IPTG at OD_{600} = 0.6
758 overnight at 16°C. Cells were harvested by centrifugation and the pellet was
759 resuspended in Lysis Buffer (20 mM HEPES, 500 mM NaCl, 0.5 mM TCEP, 20 mM
760 imidazole, 2% glycerol, 20 mM $MgCl_2$) and flash frozen in liquid nitrogen. Pellets were
761 thawed on ice and cells were lysed by 5 passes through a high-pressure homogenizer
762 (Avestin EmulsiFlex-C3, Ottawa, Canada). The lysate was spun down at 100,000 g and
763 the soluble fraction was incubated with HisPur™ Ni-NTA Resin for 2.5 h at 4°C while
764 rotating. The bound protein was washed sequentially with Lysis Buffer, Lysis Buffer
765 containing 50 mM and finally 100 mM Imidazole. The protein was eluted in Elution
766 Buffer (20 mM HEPES, 500 mM NaCl, 0.5 mM TCEP, 200 mM Imidazole, 2% glycerol,
767 20 mM MgCl2). The protein was concentrated using a Vivaspin® with a 10 kDa
768 molecular weight cutoff and the concentration determined by Bradford protein assay.
769 His6-FisB ECD G123C was labeled with iFluor555™ maleimide dye (AAT Bioquest,
770 Sunnyvale, CA, USA) by adding a 20x molar excess of dye to the protein and the
771 reaction was incubated overnight at 4°C. Free dye was removed using a HiPrep 20/10
772 (GE, Chicago, IL, USA) column.

773

774 **Giant Unilamellar Vesicle (GUV) preparation**

775 GUVs were formed by electroformation (Stockl et al., 2010). Briefly, chloroform-
776 dissolved lipids were mixed in a glass tube at desired ratios and spotted on two indium
777 tin oxide (ITO) coated glass slides. Organic solvent was removed by placing the lipid
778 films in a vacuum desiccator for at least 2 h. A short strip of copper conductive tape was

779 attached to each ITO slide which are then separated by a PTFE spacer and held
780 together with binder clips. The chamber was filled with 500 µl Swelling Buffer (SweBu, 1
781 mM HEPES, 0.25 M sucrose, 1 mM DTT) and sealed with Critoseal (McCormick
782 Scientific LLC, Saint Louis, MO, USA). GUVs were formed by applying a sinusoidal
783 voltage of 10 Hz and an amplitude of 1.8 V for at least 2 h at room temperature. GUV
784 membranes were labeled by including 1 mole % 1,2-dioleoyl-sn-glycero-3-
785 phosphoethanolamine-N-(7-nitro-2-1,3-benzoxadiazol-4-yl) (NBD-PE) or 1,1'-
786 dioctadecyl-3,3,3',3'-tetramethylindodicarbocyanine perchlorate (DiD) in the lipid
787 composition. In **Figure 2**, "100% PC" and "30% CL" membranes are composed of (all
788 mole %) 99% phosphatidylcholine (PC), 1% NBD-PE, and 30% *E. coli* cardiolipin (CL),
789 69% eggPC, 1% NBD-PE, respectively. Deflated GUVs were composed of (all mole %)
790 25% *E. coli* phosphatidylethanolamine (PE), 5% *E. coli* CL, 50% *E. coli*
791 phosphatidylglycerol (PG), 19% eggPC and 1% DiD or NBD-PE (BS mix). All lipids were
792 purchased from Avanti Polar Lipids (Alabaster, AL), except for DiD which was from
793 Thermo Fisher (Waltham, MA).

794 GUVs were imaged using a Nikon Eclipse TE2000-E microscope. Prior to adding the
795 GUVs, the imaging chamber was filled with a 5 mg/ml β-Casein (Sigma, Saint Louis, MI,
796 USA) solution to prevent attachment of the GUVs to the glass coverslip. The β-Casein
797 solution was removed and replaced with RB-EDTA.

798

799 **Fluorescence recovery after photobleaching (FRAP)**

800 FRAP measurements were conducted using a Leica SP8 inverted microscope in the
801 same open imaging chamber. As described above GUVs were diluted in RB-EDTA (25
802 mM HEPES at pH 7.4, 850140 mM KCl, 1 mM EDTA, 0.2 mM tris(2-carboxyethyl)
803 phosphine) and incubated with 1 µM FisB ECD for 2-3h. A rectangular area was chosen
804 to bleach as indicated in Figure 2C. Five images (laser power 0.7%) were recorded
805 before bleaching, 10 during bleaching (laser power 100%) and 60 after bleaching (laser
806 power 0.7%).

807 The mean GUV intensity was determined using ImageJ. A segmented line (10 pixels
808 wide) was drawn to manually follow the GUV membrane. The line was smoothed using
809 'fit spine' and the mean pixel intensity was calculated. The background was determined
810 as the mean pixel value of a 20 x 20-pixel box (close to but outside the GUVs) and
811 subtracted from the mean pixel intensity of the GUVs.

812

813 **Image analysis**

814 **Determination of forespore and mother membrane surface area.** Using the ImageJ
815 plugin Filament 2D (Smith et al., 2010), "snakes" were fitted to forespores and mother
816 cells (Figure S1A). Snakes were fitted to forespores using either the TMA-DPH
817 membrane stain (using ridges) or a soluble CFP marker (using gradients) expressed in
818 the forespores. Snakes were fitted to mother cells using the corresponding phase
819 contrast image using gradients. In all cases the snakes were fitted as contours. Fitting
820 parameters were as follows: $\alpha = 100$, $\beta = 100$, $\gamma = 800$, weight=0.5, stretch force=100,
821 deform iterations=50, point spacing=0.5, image smoothing=1.01.

822 To determine the surface area of forespores and mother cells, the snakes were then
823 further analyzed with MATLAB. First, an ellipse was fitted to the snakes to determine
824 the symmetry axis of the forespore or mother cell (Figure S1B). Half of the snake is then
825 rotated around the symmetry axis to create a surface of revolution from which the
826 membrane surface area for the forespore or mother cell was determined (Figure S1C).

827 For the analyses shown in **Figure *5***l, FisB foci were semi-automatically selected using
828 SpeckleTrackerJ (Smith et al., 2011). For each spot, the sum of pixel values in a 6
829 pixels × 6 pixels (0.5 μm×0.5 μm) box around the center of the spot were calculated.
830 For each corresponding cell, the same operation was performed at a membrane area
831 where no clusters were present and subtracted from the individual FisB cluster intensity.

832 **Determination of mean fluorescence intensity around the forespore.** We used
833 ImageJ plugin Filament 2D to fit snakes around forespores (see above) to define
834 forespore contours. Mean contour intensity was calculated using Matlab, using snake
835 coordinates from Filament 2D**.**

836

837 **Modeling.** Please see SI Appendix for details.

838

SUPPLEMENTARY FIGURE LEGENDS

Figure S1. Forespore area changes can also be detected using a soluble marker. Related to Figure 3. A. Membrane fission was assessed by fluorescent microscopy during a sporulation time course in wild type (BKM015) cells containing a fluorescent forespore reporter (P_{spoIIQ}-*cfp*). Membranes were visualized with the fluorescent dye TMA-DPH. Forespore contours in pre- and post-fission cells are indicated with blue or red contours, respectively. Time (in hours) after the initiation of sporulation is indicated as T2.5, T.3, etc.. Bar, 1 µm. **B.** Average post-fission forespore areas (A_{FS}) detected using either marker grow while average pre-fission FS areas shrink as a function of time into sporulation. Error bars represent SEM from three independent experiments (70 cells were analyzed per point).

Figure S2. Blocking lipid synthesis inhibits forespore inflation and membrane fission. Related to Figure 4. A. Cerulenin (Cer) inhibits *de novo* synthesis of neutral lipids and phospholipids by inhibiting *de novo* fatty acid biosynthesis. **B.** Representative images showing cells at *t* = 3 h after addition of 10 µg/ml cerulenin at indicated timepoints after nutrient downshift. Membranes were visualized with TMA-DPH. A cell that is blocked at the asymmetric division stage is highlighted (red arrowhead). Scale bars = 1 µm**. C.** Percentage of cells (wild-type strain, PY79) that have undergone membrane fission at *t* = 3 h after addition of cerulenin at the indicated timepoints. More than 300 cells were analyzed for each time point. **D**. Quantification of forespore membrane area for cells that have (red) or have not (blue) undergone membrane fission at *t* = 3 h after cerulenin addition at the indicated times after nutrient downshift (n=25-70 cells per data point). **E.** Fractional area occupied by the FS in pre- (blue) and post-fission (red) cells at t = 3 h. Cerulenin was added at the indicated times after nutrient downshift (n=25-70 cells per data point). **F**. Representative images showing cells (strain BAM003) at t=3 hr after the nutrient downshift, with Cer application for the indicated durations. Examples of cells with a discrete mGFP-FisB focus at the cell pole are highlighted with green arrowheads. Scale bars represent 1 µm. **G.** Engulfment is perturbed to a greater extent when lipid synthesis is inhibited earlier by cerulenin addition (>300 cells per data point). **H**. Percentage of cells with FisB accumulation (ISEP formation) at the membrane fission site, for cells that have visually completed engulment. **I**. The fraction of post-fission cells among cells with correct FisB localization (ISEP formation) as a function of increasing cerulenin application time (n=90-200 cells were analyzed per point). Means$\pm$SEM of 3 independent experiments are shown for panels C-E and G-I.

Figure S3. Blocking forespore inflation inhibits membrane fission. Related to Figure 4. A. Engulfment and FisB localization in cells expressing wild-type (WT) SpoIIIE or ATP-ase deficient SpoIIIE36. Membranes were labeled with TMA-DPH and FisB was visualized using mGFP-FisB expressed at native levels on a *ΔfisB* background (Landajuela et al., 2021). Fluorescence microscopy images were acquired 3 h after nutrient downshift that initiated sporulation. Cells that have visually completed engulfment and had accumulated FisB a the membrane fission site are indicated by arrowheads. On the images on the right, detected FS contours are overlaid in blue and

red for pre- and post-fission cells. **B**. Percentage of cells that underwent membrane fission as a function of time into sporulation, for WT and SpoIIIE36 cells. (For each data point >300 cells were analyzed). **C**. FS areas as a function of time after nutrient downshift, for pre- (blue) and post-fission (red) cells, expressing either WT (solid lines) or ATPase deficient SpoIIIE (SpoIIIE36). (n=25-70 cells per data point) **D-F**. As in A-C, but using cells expressing mGFP-FisB at ~8-fold lower levels (Landajuela et al., 2021). **G**. FisB localization is affected when DNA translocation is completely blocked. Percentage of cells displaying an intense spot at the engulfment pole (ISEP) for cells expressing SpoIIIE^{WT} or SpoIIIE36 on a background with either native or reduced mGFP-FisB levels. Scale bars = 1 μm. **H.** The fraction of post-fission cells among cells with correct FisB localization (ISEP formation). (n=25-70 cells were analyzed per data point). In panels B,C, E-H, mean±SEM of three independent biological replicates are plotted for every point.

Figure S4. Pre-fission forespores inflate in a low expression FisB strain in which membrane fission is delayed. Related to Figure 5. A. Summary of FisB copy number quantification under native or low expression levels (Landajuela et al., 2021). Right. Under native expression, on average, there are ~1,000 FisB molecules per cell at t=3 h. Each DMC contains ~12 FisB molecules, while the ISEP contains ~40 FisB copies. In the low-expression strain all the numbers are scaled down ~7-8-fold. **B.** Time course of membrane fission for wild-type cells, *ΔfisB* cells, or *ΔfisB* cells complemented with mGFP-FisB expressed at native (BAM003) or low levels (BAL003). (More than 300 cells were analyzed per data point.) **C.** Fluorescence microscopy images of cells expressing mGFP-FisB at the native level (BAM003) at 3 h into sporulation. Membranes were visualized with TMA-DPH. Examples of a sporulating cell with a discrete mGFP-FisB focus at the cell pole (intense spot at engulfment pole, ISEP) are highlighted with a red arrowhead. In the panels on the right red contours indicate forespores that have undergone fission whereas blue contours indicate forespores that have not yet undergone membrane fission (70 cells per data point). Scale bars represent is 1 μm. **D.** Similar to C but using a strain (BAL003) that expresses mGFP-FisB at lower levels in a *ΔfisB* background. **E, F.** Under mGFP-FisB expression at low levels, both the average pre- (E) and post-fission (F) forespore areas (A_{FS}) grow, in a manner qualitatively similar to cells lacking FisB altogether (ΔFisB). By contrast, for cells expressing mGFP-FisB the native level, the average pre- and post-fission FS areas decrease and increase as a function of time into sporulation, respectively (70 cells were analyzed per data point). Data for *ΔfisB* cells is copied from Figure 6 for comparison. In panels B, E, F, mean±SEM of three independent replicates are plotted.

Figure S5. Examples of forespore area growth and membrane fission detected at the single cell level. Related to Figure 6. Each top row of a triplet shows a unique cell followed as a function of time in time-lapse fluorescence microscopy. Cell membranes were labeled with FM4-64. Images are shown with an inverted look-up table. Frames were acquired every 5 min. The middle and bottom rows of every triplet shows the overlaid contour of the FS or the MC membrane, respectively. The intensity of the FS

924 membrane starts decreasing upon membrane fission, because bleached FM4-64
925 molecules are confined and can no longer exchange with the unlabeled dyes in the bath
926 after membrane fission. For each cell, the mean FS contour intensity and the FS area
927 are shown on the right. The time of membrane fission (τ_{fiss}) estimated from the contour
928 intensity time profile is indicated on the FS area plots.

929

930

931

932 **REFERENCES**

933 Allemand, J.F., and Maier, B. (2009). Bacterial translocation motors investigated by single
934 molecule techniques. FEMS Microbiol Rev *33*, 593-610.

935 Bath, J., Wu, L.J., Errington, J., and Wang, J.C. (2000). Role of Bacillus subtilis SpoIIIE
936 in DNA transport across the mother cell-prespore division septum. Science *290*, 995-997.

937 Boron, W., and Boulpaep, E. (2017). Medical Physiology, 3 edn (Philadelphia, PA:
938 Elsevier).

939 Burton, B.M., Marquis, K.A., Sullivan, N.L., Rapoport, T.A., and Rudner, D.Z. (2007). The
940 ATPase SpoIIIE transports DNA across fused septal membranes during sporulation in
941 Bacillus subtilis. Cell *131*, 1301-1312.

942 Campelo, F., and Malhotra, V. (2012). Membrane fission: the biogenesis of transport
943 carriers. Annu Rev Biochem *81*, 407-427.

944 Cochilla, A.J., Angleson, J.K., and Betz, W.J. (1999). Monitoring secretory membrane
945 with FM1-43 fluorescence. Annu Rev Neurosci *22*, 1-10.

946 Doan, T., Coleman, J., Marquis, K.A., Meeske, A.J., Burton, B.M., Karatekin, E., and
947 Rudner, D.Z. (2013). FisB mediates membrane fission during sporulation in Bacillus
948 subtilis. Genes Dev *27*, 322-334.

949 Evans, E., Heinrich, V., Ludwig, F., and Rawicz, W. (2003). Dynamic tension
950 spectroscopy and strength of biomembranes. Biophysical Journal *85*, 2342-2350.

951 Ferguson, S.M., and De Camilli, P. (2012). Dynamin, a membrane-remodelling GTPase.
952 Nat Rev Mol Cell Biol *13*, 75-88.

953 Heath, R.J., and Rock, C.O. (2004). Fatty acid biosynthesis as a target for novel
954 antibacterials. Curr Opin Investig Drugs *5*, 146-153.

955 Karatekin, E., Sandre, O., Guitouni, H., Borghi, N., Puech, P.H., and Brochard-Wyart, F.
956 (2003). Cascades of transient pores in giant vesicles: line tension and transport. Biophys
957 J *84*, 1734-1749.

958 Khanna, K., Lopez-Garrido, J., Zhao, Z., Watanabe, R., Yuan, Y., Sugie, J., Pogliano, K.,
959 and Villa, E. (2019). The molecular architecture of engulfment during Bacillus subtilis
960 sporulation. Elife *8*.

961 Landajuela, A., Braun, M., Rodrigues, C.D.A., Martinez-Calvo, A., Doan, T., Horenkamp,
962 F., Andronicos, A., Shteyn, V., Williams, N.D., Lin, C.X.*, et al.* (2021). FisB relies on homo-
963 oligomerization and lipid binding to catalyze membrane fission in bacteria. Plos Biol *19*.

964 Liu, N., Chistol, G., and Bustamante, C. (2015). Two-subunit DNA escort mechanism and
965 inactive subunit bypass in an ultra-fast ring ATPase. Elife *4*.

966 Liu, N., Chistol, G., Cui, Y., and Bustamante, C. (2018). Mechanochemical coupling and
967 bi-phasic force-velocity dependence in the ultra-fast ring ATPase SpoIIIE. Elife *7*.

968 Liu, N.J., Dutton, R.J., and Pogliano, K. (2006). Evidence that the SpoIIIE DNA
969 translocase participates in membrane fusion during cytokinesis and engulfment. Mol
970 Microbiol *59*, 1097-1113.

971 Lopez-Garrido, J., Ojkic, N., Khanna, K., Wagner, F.R., Villa, E., Endres, R.G., and
972 Pogliano, K. (2018). Chromosome Translocation Inflates Bacillus Forespores and
973 Impacts Cellular Morphology. Cell *172*, 758-770 e714.

974 Moir, A., and Cooper, G. (2015). Spore Germination. Microbiol Spectr *3*.

975 Needham, D., and Nunn, R.S. (1990). Elastic-Deformation and Failure of Lipid Bilayer-
976 Membranes Containing Cholesterol. Biophysical Journal *58*, 997-1009.

977 Ojkic, N., Lopez-Garrido, J., Pogliano, K., and Endres, R.G. (2014). Bistable Forespore
978 Engulfment in Bacillus subtilis by a Zipper Mechanism in Absence of the Cell Wall. Plos
979 Comput Biol *10*, e1003912.

980 Ojkic, N., López-Garrido, J., Pogliano, K., and Endres, R.G. (2016). Cell-wall remodeling
981 drives engulfment during Bacillus subtilis sporulation. Elife *5*.

982 Pedrido, M.E., de Ona, P., Ramirez, W., Lenini, C., Goni, A., and Grau, R. (2013). Spo0A
983 links de novo fatty acid synthesis to sporulation and biofilm development in Bacillus
984 subtilis. Mol Microbiol *87*, 348-367.

985 Pogliano, K., Hofmeister, A.E., and Losick, R. (1997). Disappearance of the sigma E
986 transcription factor from the forespore and the SpoIIE phosphatase from the mother cell
987 contributes to establishment of cell-specific gene expression during sporulation in Bacillus
988 subtilis. J Bacteriol *179*, 3331-3341.

989 Renard, H.F., Johannes, L., and Morsomme, P. (2018). Increasing Diversity of Biological
990 Membrane Fission Mechanisms. Trends Cell Biol *28*, 274-286.

991 Schoneberg, J., Lee, I.H., Iwasa, J.H., and Hurley, J.H. (2017). Reverse-topology
992 membrane scission by the ESCRT proteins. Nat Rev Mol Cell Biol *18*, 5-17.

993 Schujman, G.E., Grau, R., Gramajo, H.C., Ornella, L., and de Mendoza, D. (1998). De
994 novo fatty acid synthesis is required for establishment of cell type-specific gene
995 transcription during sporulation in Bacillus subtilis. Mol Microbiol *29*, 1215-1224.

996 Setlow, P. (2003). Spore germination. Current Opinion in Microbiology *6*, 550-556.

997 Sharp, M.D., and Pogliano, K. (1999). An in vivo membrane fusion assay implicates
998 SpoIIIE in the final stages of engulfment during Bacillus subtilis sporulation. Proc Natl
999 Acad Sci U S A *96*, 14553-14558.

1000 Simunovic, M., Evergren, E., Callan-Jones, A., and Bassereau, P. (2019). Curving Cells
1001 Inside and Out: Roles of BAR Domain Proteins in Membrane Shaping and Its Cellular
1002 Implications. Annu Rev Cell Dev Biol *35*, 111-129.

1003 Simunovic, M., Manneville, J.B., Renard, H.F., Evergren, E., Raghunathan, K., Bhatia,
1004 D., Kenworthy, A.K., Voth, G.A., Prost, J., McMahon, H.T*., et al.* (2017). Friction Mediates
1005 Scission of Tubular Membranes Scaffolded by BAR Proteins. Cell *170*, 172-184 e111.

1006 Smith, M.B., Karatekin, E., Gohlke, A., Mizuno, H., Watanabe, N., and Vavylonis, D.
1007 (2011). Interactive, computer-assisted tracking of speckle trajectories in fluorescence
1008 microscopy: application to actin polymerization and membrane fusion. Biophys J *101*,
1009 1794-1804.

1010 Smith, M.B., Li, H., Shen, T., Huang, X., Yusuf, E., and Vavylonis, D. (2010).
1011 Segmentation and tracking of cytoskeletal filaments using open active contours.
1012 Cytoskeleton (Hoboken) *67*, 693-705.

1013 Sterlini, J.M., and Mandelstam, J. (1969). Commitment to Sporulation in Bacillus Subtilis
1014 and Its Relationship to Development of Actinomycin Resistance. Biochem J *113*, 29-+.

1015 Stockl, M., Nikolaus, J., and Herrmann, A. (2010). Visualization of lipid domain-specific
1016 protein sorting in giant unilamellar vesicles. Methods Mol Biol *606*, 115-126.

1017 Tiller, G.E., Mueller, T.J., Dockter, M.E., and Struve, W.G. (1984). Hydrogenation of triton
1018 X-100 eliminates its fluorescence and ultraviolet light absorption while preserving its
1019 detergent properties. Anal Biochem *141*, 262-266.

1020 Tocheva, E.I., Matson, E.G., Morris, D.M., Moussavi, F., Leadbetter, J.R., and Jensen,
1021 G.J. (2011). Peptidoglycan remodeling and conversion of an inner membrane into an
1022 outer membrane during sporulation. Cell *146*, 799-812.

1023 Vadia, S., Tse, J.L., Lucena, R., Yang, Z., Kellogg, D.R., Wang, J.D., and Levin, P.A.
1024 (2017). Fatty Acid Availability Sets Cell Envelope Capacity and Dictates Microbial Cell
1025 Size. Curr Biol *27*, 1757-1767 e1755.

1026 Webb, C.D., Teleman, A., Gordon, S., Straight, A., Belmont, A., Lin, D.C., Grossman,
1027 A.D., Wright, A., and Losick, R. (1997). Bipolar localization of the replication origin regions
1028 of chromosomes in vegetative and sporulating cells of B. subtilis. Cell *88*, 667-674.

1029 Wu, L.J., and Errington, J. (1994). Bacillus subtilis SpoIIIE protein required for DNA
1030 segregation during asymmetric cell division. Science *264*, 572-575.

1031 Wu, L.J., and Errington, J. (1997). Septal localization of the SpoIIIE chromosome
1032 partitioning protein in Bacillus subtilis. EMBO J *16*, 2161-2169.

1033 Wu, L.J., and Errington, J. (1998). Use of asymmetric cell division and spoIIIE mutants to
1034 probe chromosome orientation and organization in Bacillus subtilis. Mol Microbiol *27*, 777-
1035 786.

1036 Yao, Z., Davis, R.M., Kishony, R., Kahne, D., and Ruiz, N. (2012). Regulation of cell size
1037 in response to nutrient availability by fatty acid biosynthesis in *Escherichia coli*.
1038 Proceedings of the National Academy of Sciences *109*, E2561.

1039 Youngman, P.J., Perkins, J.B., and Losick, R. (1983). Genetic transposition and
1040 insertional mutagenesis in Bacillus subtilis with Streptococcus faecalis transposon Tn917.
1041 Proc Natl Acad Sci U S A *80*, 2305-2309.

1042 Zhang, Y.M., and Rock, C.O. (2008). Membrane lipid homeostasis in bacteria. Nat Rev
1043 Microbiol *6*, 222-233.

1044

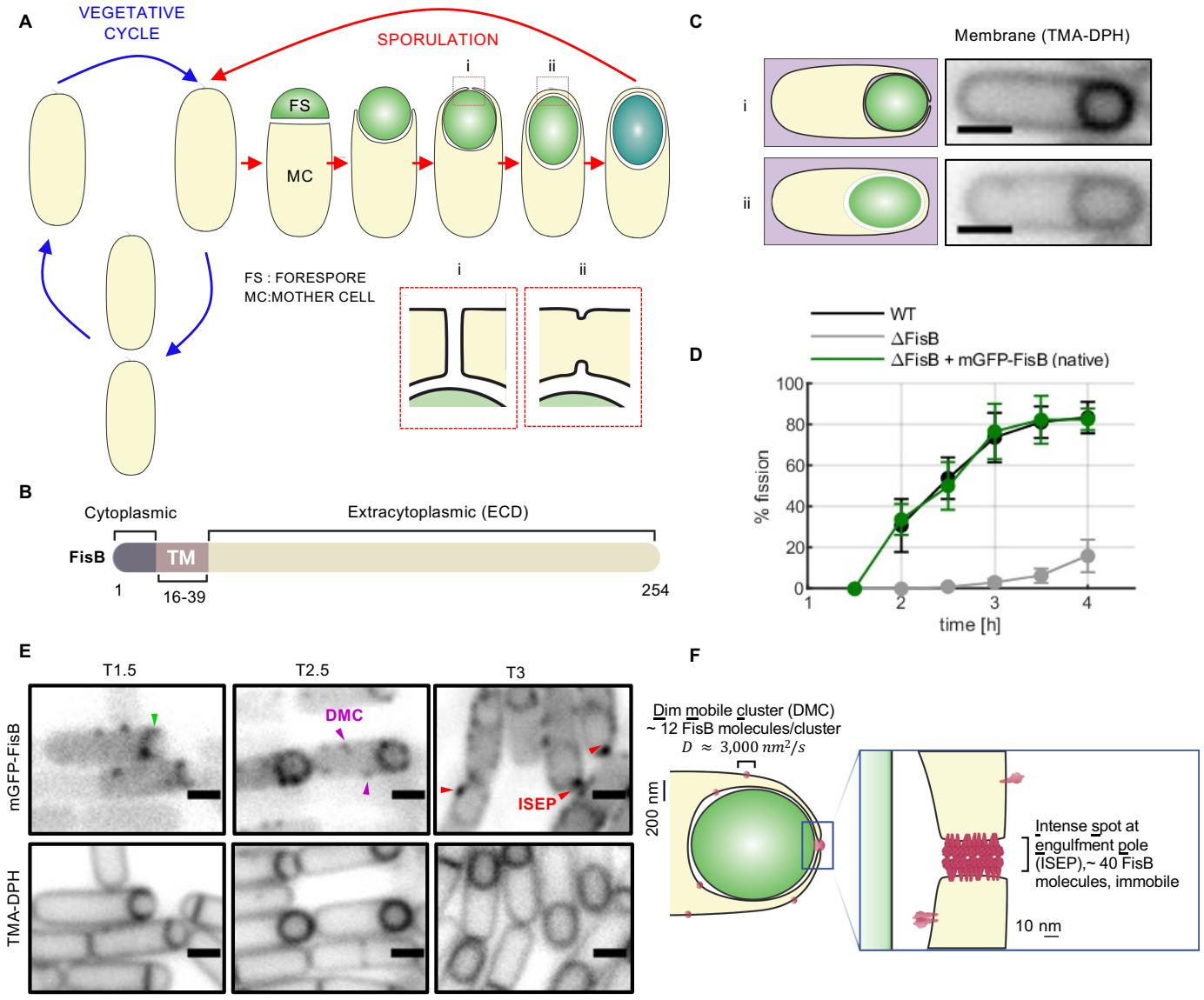
A
VEGETATIVE CYCLE
SPORULATION
FS
MC
i
ii
FS : FORESPORE
MC:MOTHER CELL
B
Cytoplasmic
Extracytoplasmic (ECD)
FisB
TM
1
16-39
254
C
Membrane (TMA-DPH)
D
WT
ΔFisB
ΔFisB + mGFP-FisB (native)
% fission
time [h]
E
T1.5
T2.5
T3
mGFP-FisB
TMA-DPH
DMC
ISEP
F
Dim mobile cluster (DMC)
~ 12 FisB molecules/cluster
$D \approx 3{,}000\ nm^2/s$
200 nm
Intense spot at engulfment pole (ISEP),~ 40 FisB molecules, immobile
10 nm

FIGURE 1

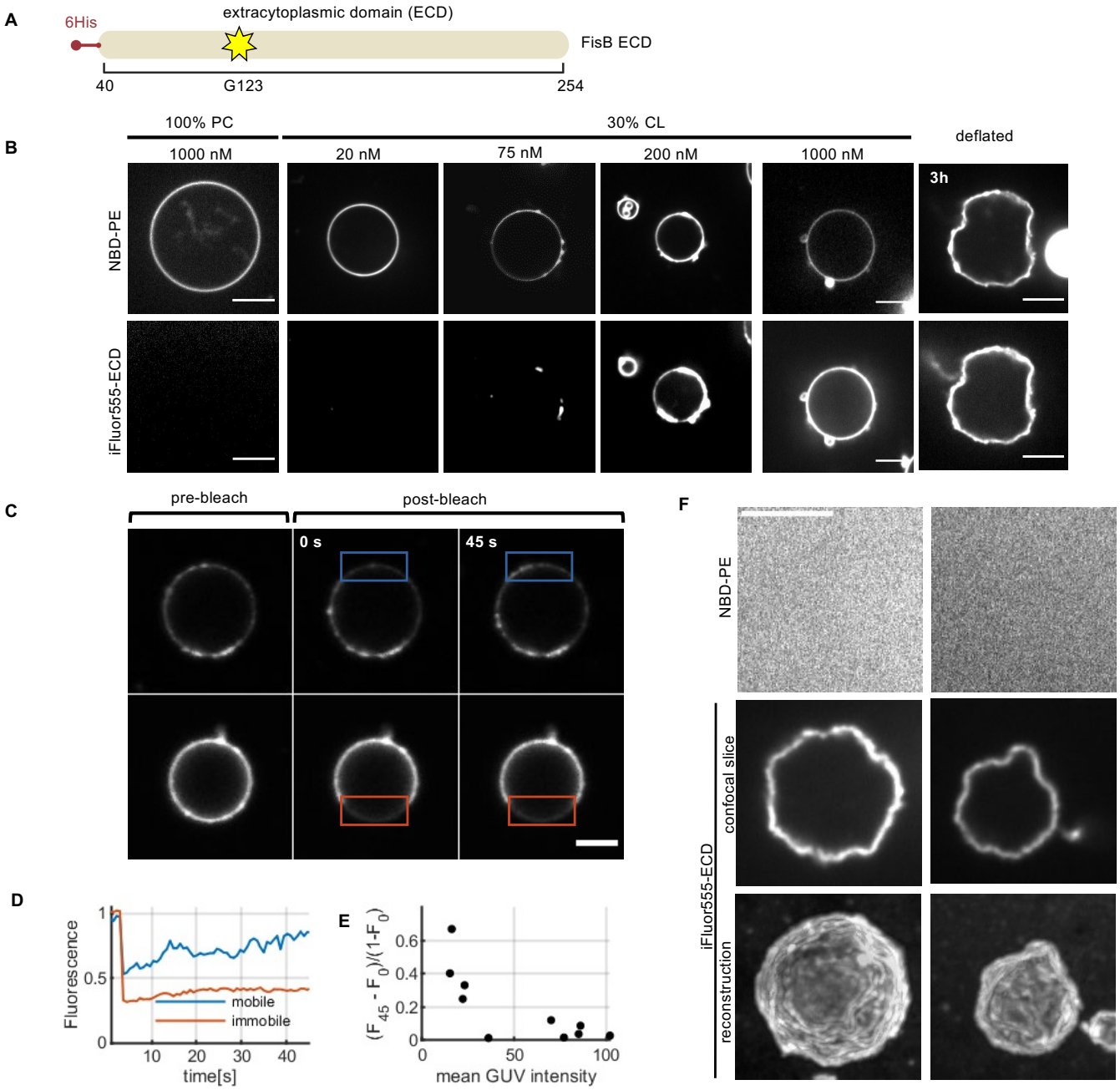
A
6His
extracytoplasmic domain (ECD)
FisB ECD
40
G123
254
B
100% PC
30% CL
deflated
1000 nM
20 nM
75 nM
200 nM
1000 nM
3h
NBD-PE
iFluor555-ECD
C
pre-bleach
post-bleach
0 s
45 s
D
Fluorescence
mobile
immobile
time[s]
E
$(F_{45} - F_0)/(1-F_0)$
mean GUV intensity
F
NBD-PE
iFluor555-ECD
confocal slice
reconstruction

FIGURE 2

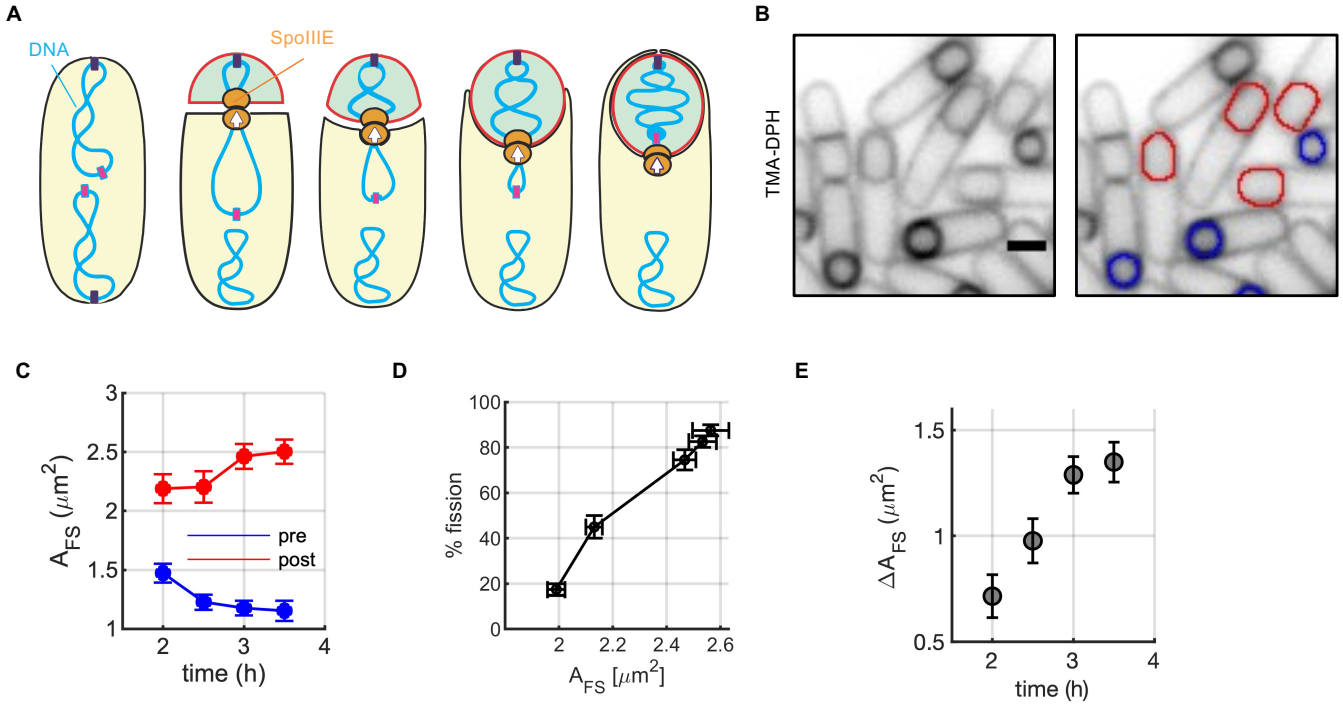
A
DNA
SpoIIIE
B
TMA-DPH
C
A_{FS} (μm^2)
time (h)
pre
post
D
% fission
A_{FS} [μm^2]
E
ΔA_{FS} (μm^2)
time (h)

FIGURE 3

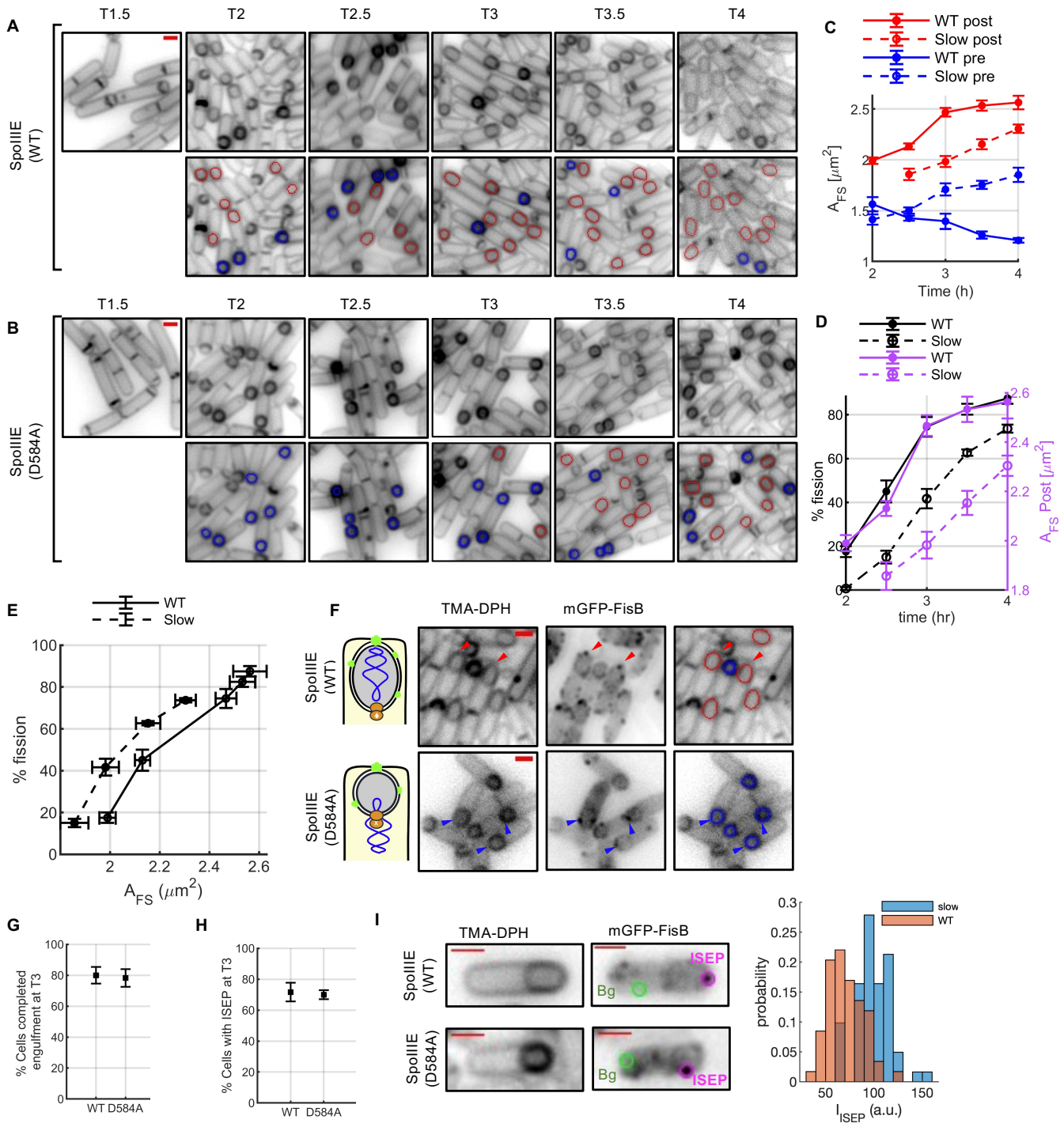
A
T1.5
T2
T2.5
T3
T3.5
T4
SpoIIIE (WT)
B
SpoIIIE (D584A)
C
WT post
Slow post
WT pre
Slow pre
A_{FS} [μm^2]
Time (h)
D
WT
Slow
WT
Slow
% fission
A_{FS} Post [μm^2]
time (hr)
E
WT
Slow
% fission
A_{FS} (μm^2)
F
TMA-DPH
mGFP-FisB
SpoIIIE (WT)
SpoIIIE (D584A)
G
% Cells completed engulfment at T3
WT D584A
H
% Cells with ISEP at T3
WT D584A
I
TMA-DPH
mGFP-FisB
SpoIIIE (WT)
SpoIIIE (D584A)
ISEP
Bg
slow
WT
probability
I_{ISEP} (a.u.)

FIGURE 4

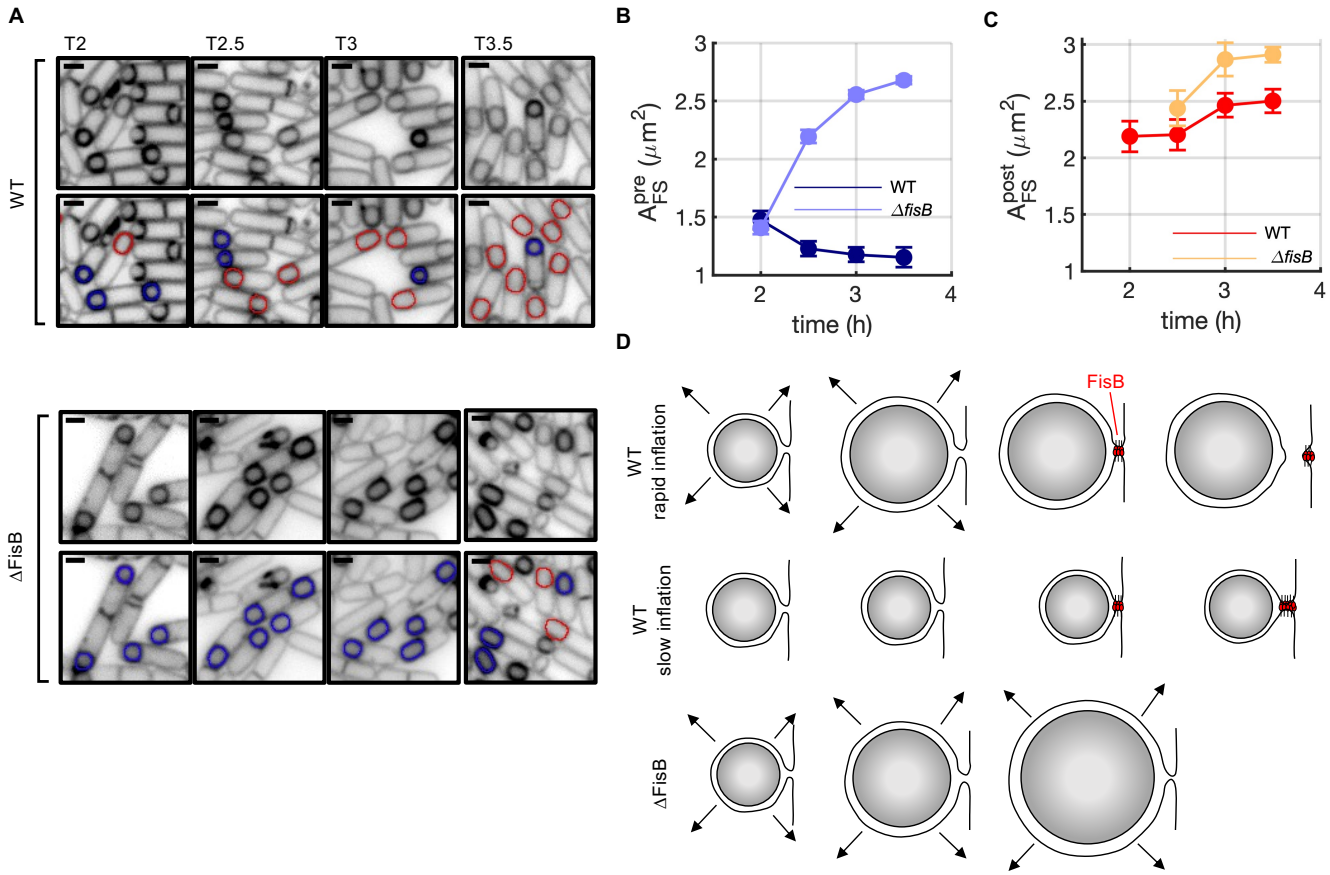
A
T2
T2.5
T3
T3.5
WT
ΔFisB
B
A_{FS}^{pre} (μm^2)
time (h)
WT
ΔfisB
C
A_{FS}^{post} (μm^2)
time (h)
WT
ΔfisB
D
WT rapid inflation
FisB
WT slow inflation
ΔFisB

FIGURE 5

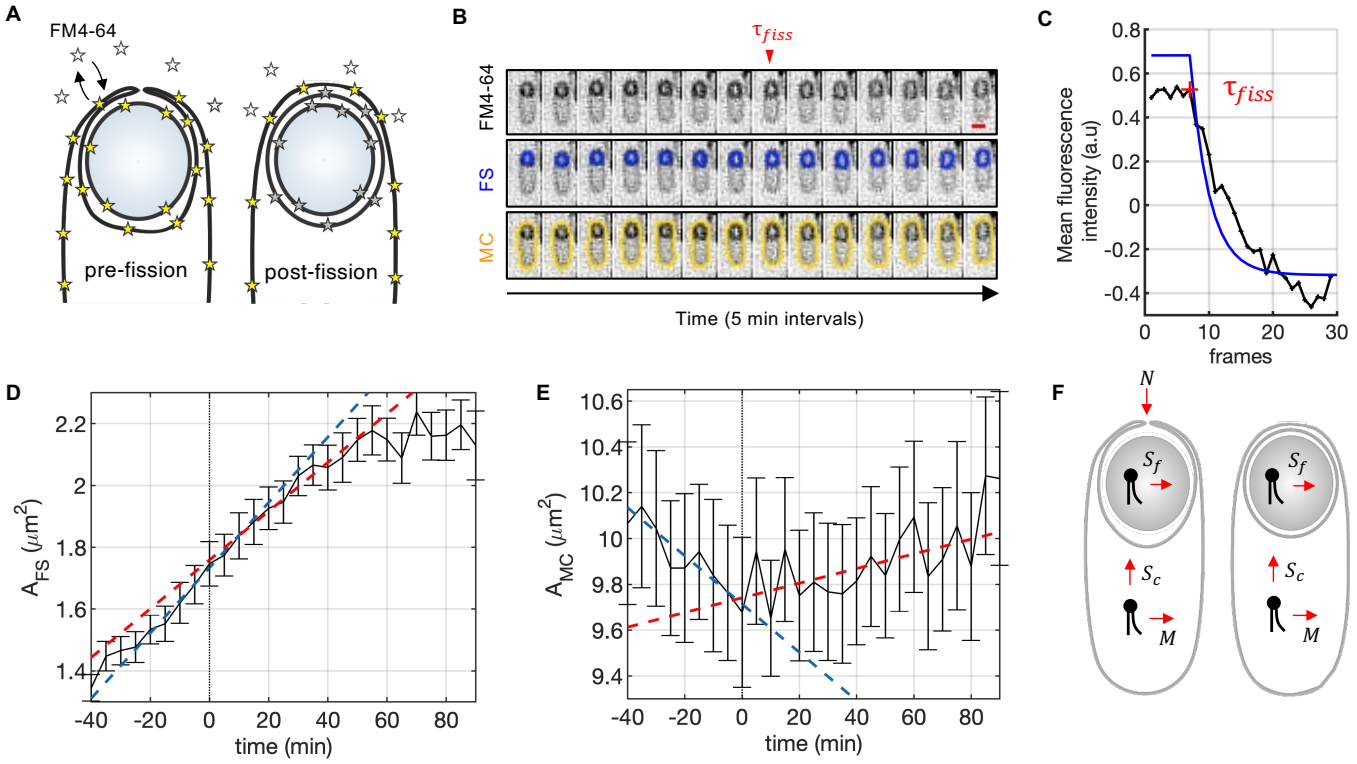
A
FM4-64
pre-fission
post-fission
B
τ_{fiss}
FM4-64
FS
MC
Time (5 min intervals)
C
Mean fluorescence intensity (a.u)
τ_{fiss}
frames
D
A_{FS} (μm^2)
time (min)
E
A_{MC} (μm^2)
time (min)
F
N
S_f
S_c
M

FIGURE 6

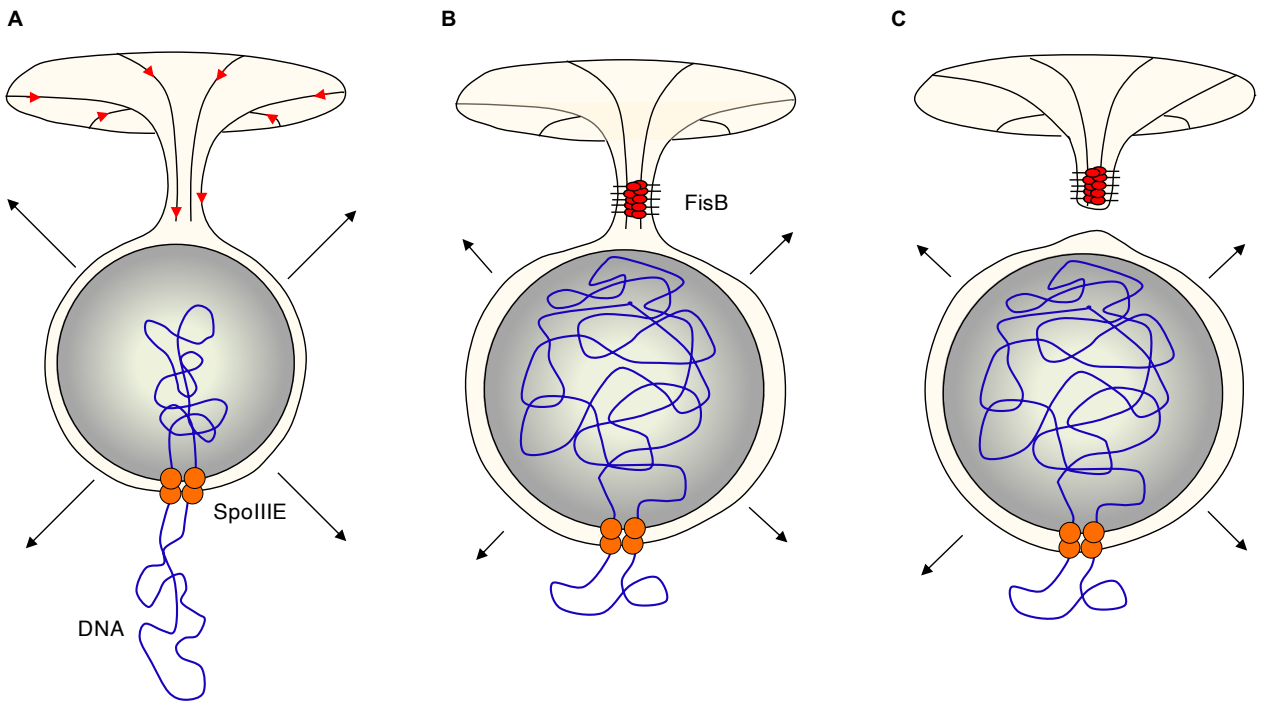

FIGURE 7

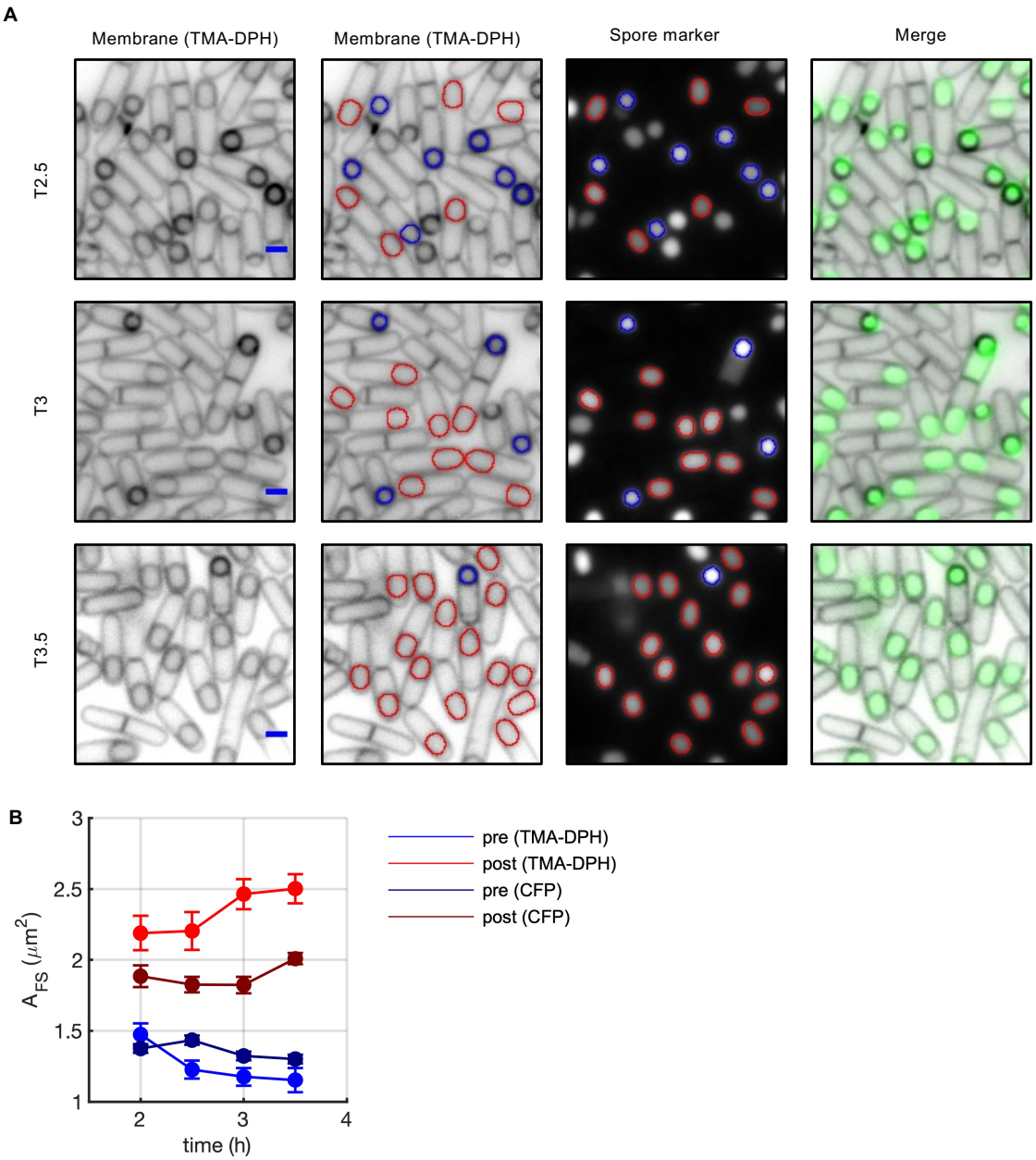
A
Membrane (TMA-DPH)
Membrane (TMA-DPH)
Spore marker
Merge
T2.5
T3
T3.5
B
3
2.5
2
1.5
1
A_{FS} (μm^2)
2
3
4
time (h)
pre (TMA-DPH)
post (TMA-DPH)
pre (CFP)
post (CFP)

FIGURE S1

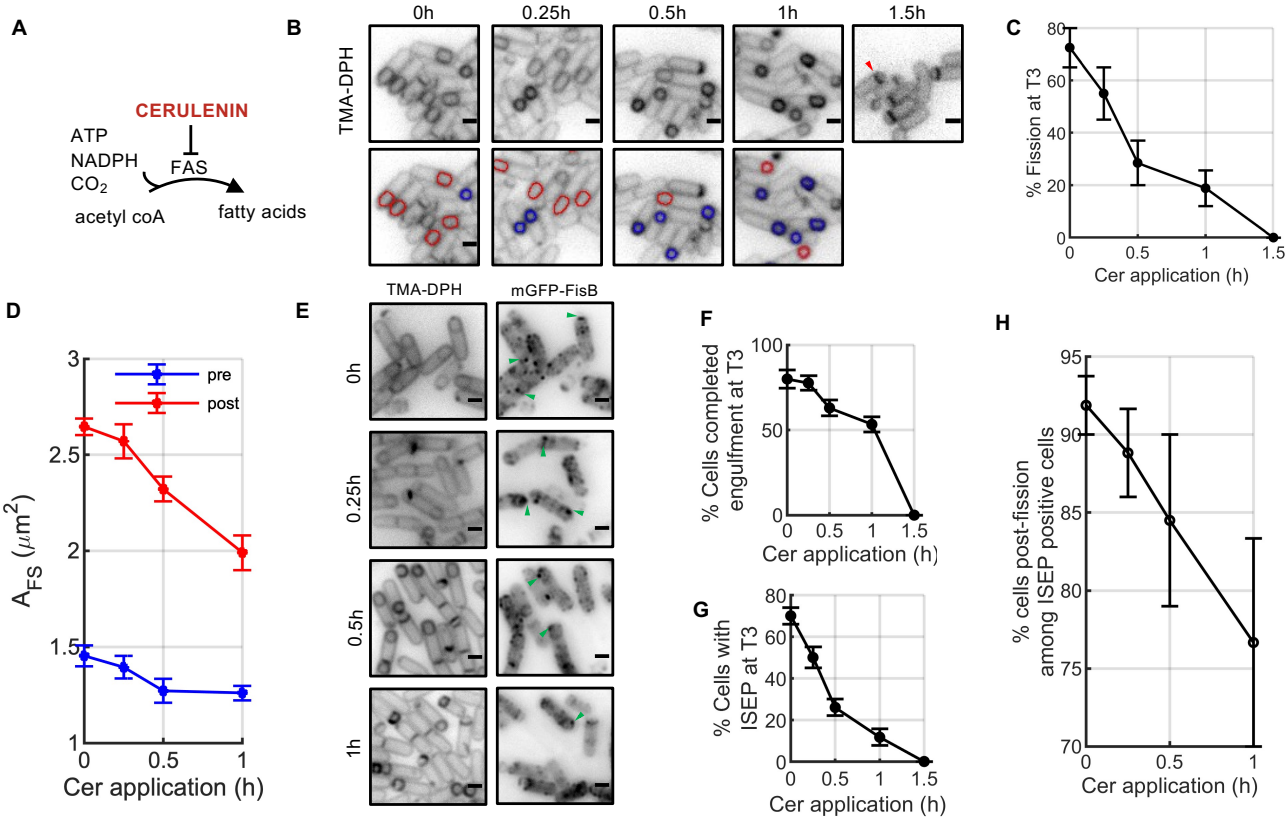
A
CERULENIN
ATP
NADPH
CO_2
FAS
acetyl coA
fatty acids
B
0h
0.25h
0.5h
1h
1.5h
TMA-DPH
C
% Fission at T3
Cer application (h)
D
pre
post
A_{FS} (μm^2)
Cer application (h)
E
TMA-DPH
mGFP-FisB
0h
0.25h
0.5h
1h
F
% Cells completed engulfment at T3
Cer application (h)
G
% Cells with ISEP at T3
Cer application (h)
H
% cells post-fission among ISEP positive cells
Cer application (h)

FIGURE S2

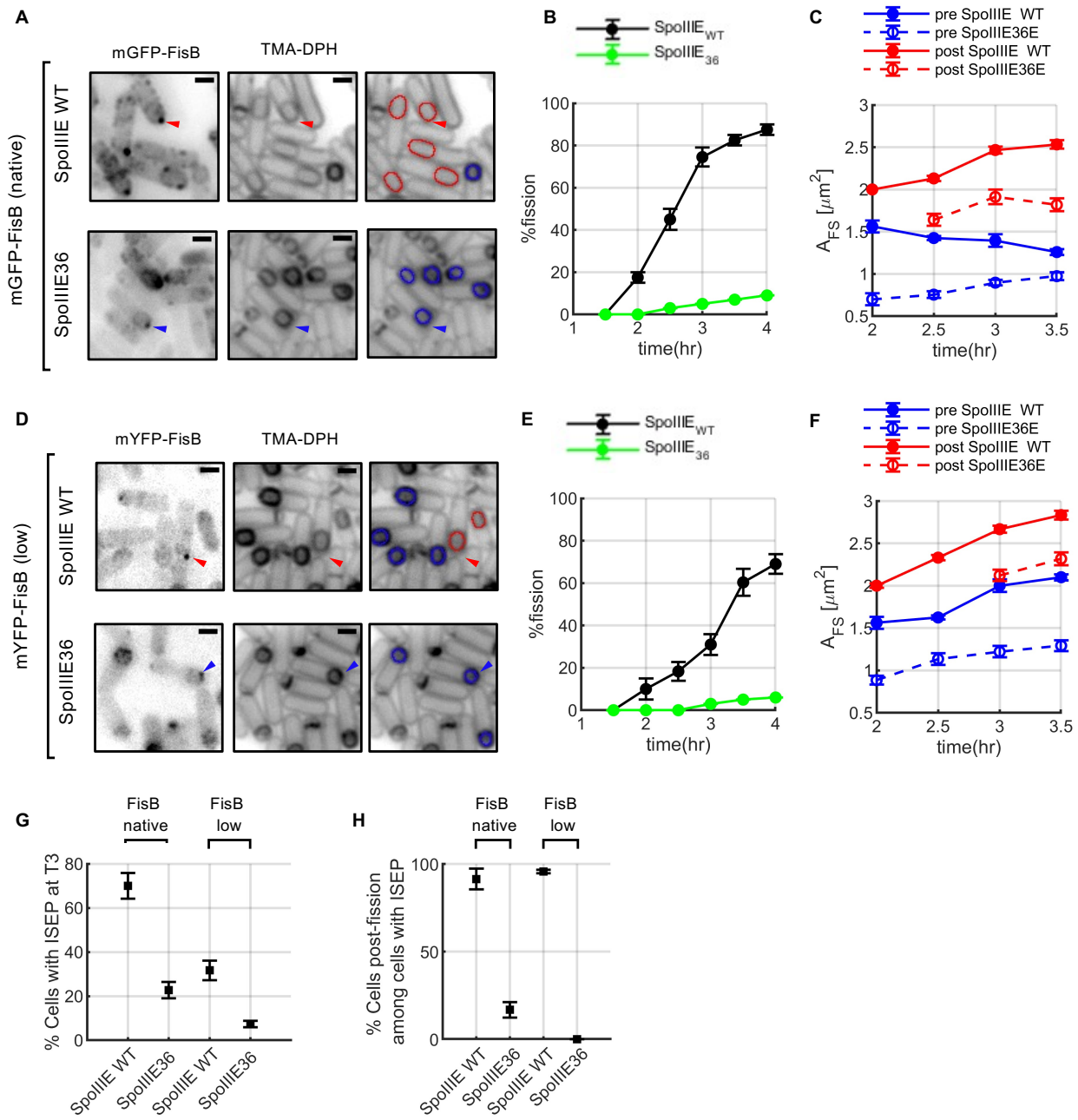
A
mGFP-FisB
TMA-DPH
mGFP-FisB (native)
SpoIIIE WT
SpoIIIE36
B
SpoIIIE$_{WT}$
SpoIIIE$_{36}$
%fission
time(hr)
C
pre SpoIIIE WT
pre SpoIIIE36E
post SpoIIIE WT
post SpoIIIE36E
A_{FS} [μm^2]
time(hr)
D
mYFP-FisB
TMA-DPH
mYFP-FisB (low)
SpoIIIE WT
SpoIIIE36
E
SpoIIIE$_{WT}$
SpoIIIE$_{36}$
%fission
time(hr)
F
pre SpoIIIE WT
pre SpoIIIE36E
post SpoIIIE WT
post SpoIIIE36E
A_{FS} [μm^2]
time(hr)

G
FisB native
FisB low
% Cells with ISEP at T3
SpoIIIE WT
SpoIIIE36
SpoIIIE WT
SpoIIIE36
H
FisB native
FisB low
% Cells post-fission among cells with ISEP
SpoIIIE WT
SpoIIIE36
SpoIIIE WT
SpoIIIE36

FIGURE S3

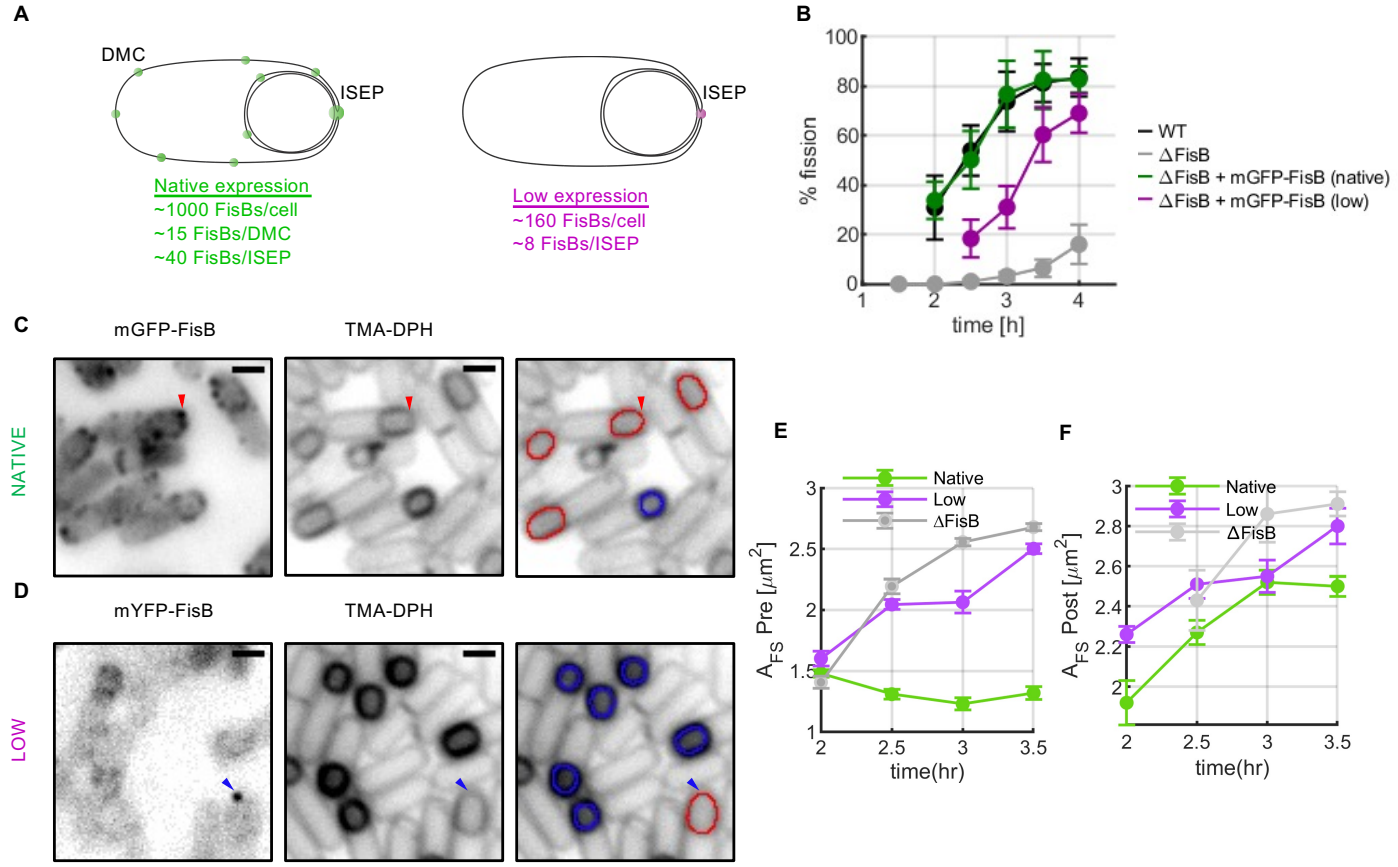
A
DMC
ISEP
Native expression
~1000 FisBs/cell
~15 FisBs/DMC
~40 FisBs/ISEP
ISEP
Low expression
~160 FisBs/cell
~8 FisBs/ISEP
B
% fission
time [h]
WT
ΔFisB
ΔFisB + mGFP-FisB (native)
ΔFisB + mGFP-FisB (low)
C
mGFP-FisB
TMA-DPH
NATIVE
D
mYFP-FisB
TMA-DPH
LOW
E
Native
Low
ΔFisB
time(hr)
F
Native
Low
ΔFisB
time(hr)

FIGURE S4

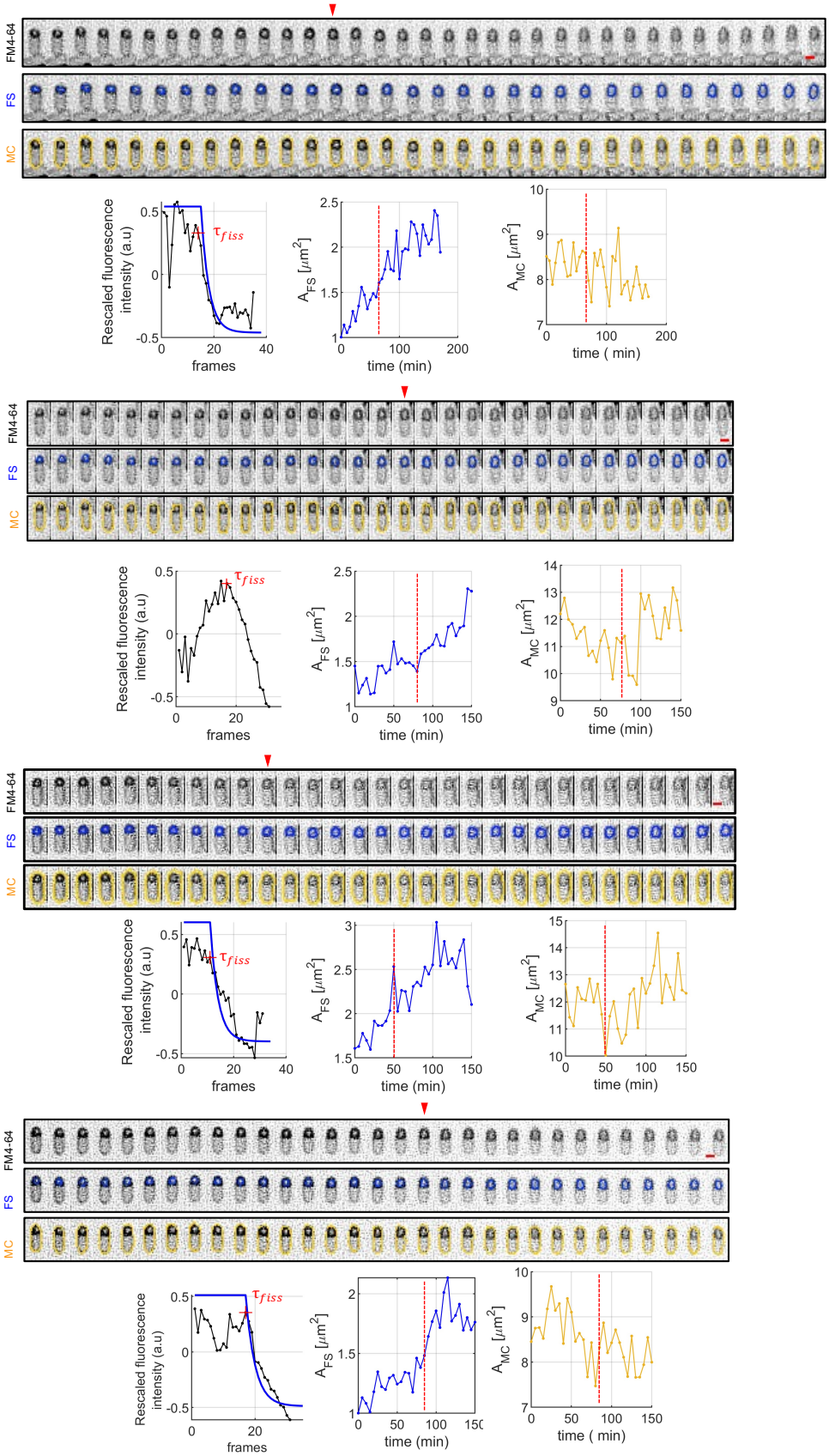
FM4-64
FS
MC
Rescaled fluorescence intensity (a.u)
frames
τ_{fiss}
A_{FS} [μm^2]
time (min)
A_{MC} [μm^2]
time (min)

FIGURE S5

SI Appendix: Theoretical Modeling

In a previous work [1] we showed that a neck of radius $\leq 5-10$ nm in the region where the engulfment membrane meets the rest of the mother cell membrane (see sketch in Fig. 1a) is necessary for FisB to accumulate. This accumulation in turn favors membrane fission, as shown in the current main text. In this appendix, first, we develop a minimal model for the neck based on free-energy minimization. This minimal model assumes a highly simplified geometry of the membrane neck, as depicted in Fig. 1(b), that accounts for membrane tension, bending, and an osmotic pressure difference, $\Delta\tilde{p} = p_{\text{cyto}} - p_{\text{peri}}$, between the cytoplasm and periplasm since the lumen of the neck is continuous with the periplasmic space. Using this model, we explore if an increase of membrane tension in the neck, e.g. due to forespore inflation, along with the osmotic pressure difference are able to narrow the radius of the neck. Then, we consider a more realistic model by solving the complete Helfrich equation [2] including the possibility of a pulling force on the neck, e.g. due to DNA translocation through the SpoIIIE motor. For this more realistic model, the shape of the membrane neck is obtained as part of the solution.

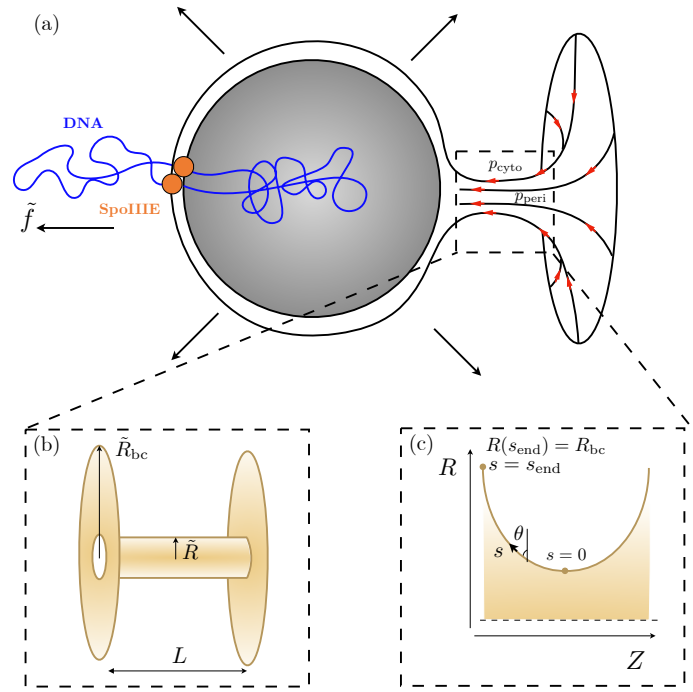

Figure 1. (a) Sketch of the engulfment membrane geometry during the last stage of forespore engulfment, showing the flow of lipids through the membrane neck, the osmotic pressure difference $\Delta\tilde{p} = p_{\text{cyto}} - p_{\text{peri}}$ between the cytoplasm and the periplasm, and the pulling force $\tilde{f}$ due to the SpoIIIE motors translocating DNA into the forespore. (b) Simplified model of the membrane neck, consisting of a straight cylinder of radius $\tilde{R}$ and length L, connecting two planar membranes of radius $\tilde{R}_{\text{bc}}$. (c) Schematic of the more realistic model of the membrane neck showing the parametrization of the surface, where s is the arc length along the contour and θ the angle with respect to the vertical.

MINIMAL MODEL FOR THE NECK: UNIFORM CYLINDER CONNECTING TWO PLANAR MEMBRANES

We first consider a highly simplified model based on the free energy $\mathscr{F}_0$ of an axisymmetric cylindrical membrane neck of radius R and length L that connects two planar membrane sheets, corresponding to the local geometry depicted in 1(b). We employ the classical Helfrich-Canham theory [2–7] for the energy of the membrane, $\mathscr{F}_0$, which reads

$$\tilde{\mathscr{F}}_0 = \int_{S_{\text{n}}} \mathrm{d}S_{\text{n}} \left[\frac{\kappa}{2}(2\tilde{H})^2 + \gamma\right] + \int_{S_{\text{s}}} \mathrm{d}S_{\text{s}}\gamma + \int_V \mathrm{d}V\Delta\tilde{p}, \qquad (1)$$

where S_{n} and S_{s} are the surfaces of the membrane neck and sheets, and V is the volume inside the neck. The tildes denote dimensional variables which will subsequently be non-dimensionalized. Here $\tilde{H}$ is the mean curvature, κ is the bending modulus, γ is the membrane surface tension, and $\Delta\tilde{p} = p_{\text{cyto}} - p_{\text{peri}}$ is the osmotic pressure difference. The two surrounding membrane sheets are assumed to be planar since their curvature is much less than that of the neck, thus their only contribution to the energy comes from their area times the membrane tension. In this simplified model, we neglect the bending energy of junctions where the cylinder meets the membrane sheets. With these simplifications, the free energy $\mathscr{F}$ in Eq. (1) reads:

$$\frac{\tilde{\mathscr{F}}_0}{2\pi} = \left(\gamma\tilde{R} + \frac{\kappa}{2\tilde{R}}\right)L + \gamma(\tilde{R}_{\text{bc}}^2 - \tilde{R}^2) + \frac{\Delta\tilde{p}}{2}\tilde{R}^2 L, \qquad (2)$$

where $\tilde{R}_{\text{bc}} > \tilde{R}$ is the outer boundary condition depicted in Fig. 1(b). Minimizing Eq. (2) with respect to the radius $\tilde{R}$ yields

$$2\gamma\tilde{R}^2 - \kappa + 2\tilde{R}^3\left(\Delta\tilde{p} - \frac{2\gamma}{L}\right) = 0. \qquad (3)$$

To non-dimensionalize Eqs. (2)–(3) we introduce the natural length scale arising from the balance between bending and tension in Eq. (1) [8] as the characteristic length scale, $R_{\text{c}} = \sqrt{\kappa/(2\gamma)}$, i.e. $R = \tilde{R}/R_{\text{c}}$. The free energy is also made dimensionless as $\mathscr{F}_0 = \tilde{\mathscr{F}}_0/(\gamma R_{\text{c}} L)$. Hence, the dimensionless forms of Eqs. (2) and (3) read:

$$\frac{\mathscr{F}_0}{2\pi} = R + \frac{1}{R} + \frac{(R_{\text{bc}}^2 - R^2)}{L/R_{\text{c}}} + \frac{\Delta p}{2}R^2, \qquad (4)$$

$$R^2 - 1 + R^3\left(\Delta p - \frac{2}{L/R_{\text{c}}}\right) = 0, \qquad (5)$$

where $\Delta p = \Delta\tilde{p}R_{\text{c}}/\gamma$.

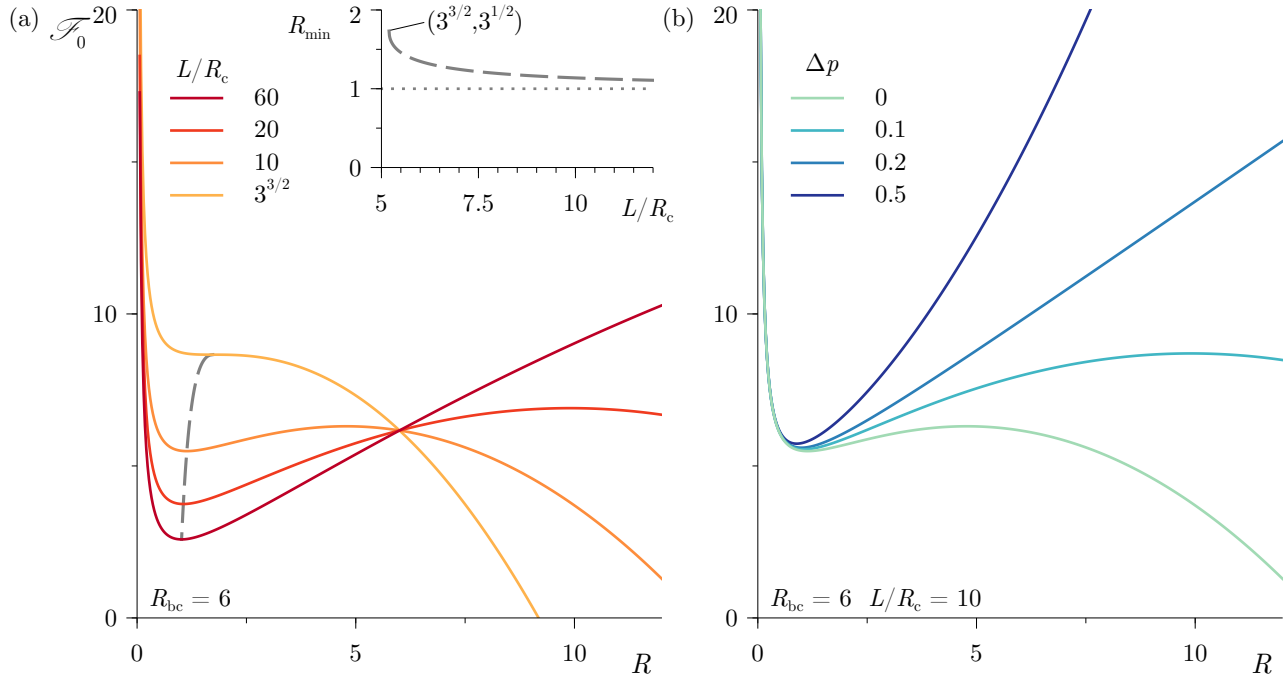

Figure 2. (a) Dimensionless free energy $\mathscr{F}_0 = \tilde{\mathscr{F}}_0/(\gamma R_c L)$ from Eq. (4) as a function of neck radius R, highlighting the existence of a local free-energy minimum provide $L/R_c > 3^{3/2}$ (gray dashed curve). Here $R_{bc} = 6$. The inset shows the corresponding radius R_{min} of the local free-energy minimum as a function of L/R_c. (b) Same as in panel (a) but for different values of the dimensionless osmotic pressure difference Δp, for a fixed length of the neck, i.e. $L/R_c = 10$.

Zero osmotic pressure difference. The solution of Eqs. (4) and (5) when $\Delta p = 0$ reveals that for a long enough neck there is a metastable state of the neck at finite radius R_{min} [9, 10]. This local minimum arises from a balance between membrane bending energy, which always favors larger R, and membrane tension, which contributes a non-monotonic function of R to the membrane energy. The existence of this local minimum can be observed in Fig. 2, which shows the dimensionless free energy $\mathscr{F}_0$ as a function of R for different values of L/R_c, along with the location R_{min} of the local minimum. Intuitively, for R around R_{min}, increasing the radius R increases the total amount of membrane in the vicinity of the neck and so increasing R is opposed by surface tension. By contrast, for larger values of R, increasing R removes more membrane from the parallel sheets (removed area scaling $\sim R^2$) than is added to the neck (added area scaling $\sim LR$), so further increase of R is energetically favored (specifically when $R > \sqrt{3} + \sqrt{2}\sqrt{L/R_c - 3\sqrt{3}}/3^{3/4} + O(L/R_c)$). We find that, for lengths below a critical value $L/R_c < 3^{3/2}$, the energy functional $\mathscr{F}_0$ does not have a local minimum, so that expanding the radius of the neck always decreases the total energy of the system, implying the neck opens.

Finite osmotic pressure difference. Eq. (5) indicates that a positive osmotic pressure difference between the cytoplasm and the periplasm favors the formation of a locally stable, narrow membrane neck. Indeed, the critical neck length below which there is no locally stable narrow neck decreases as Δp increases, $L/R_c \leq 2 \cdot 3^{3/2}/(2 + 3^{3/2}\Delta p)$. Moreover, the local maxima shown in Fig. 2(a) for $\Delta p = 0$, disappears when $\Delta p > 2/(L/R_c)$, as shown in Fig. 2(b). This implies that the free energy $\mathscr{F}_0$ increases monotonically beyond the local minimum thereby the neck does not open up. Moreover, the minimum radius of the neck R_{min} always decreases as Δp increases.

EQUILIBRIUM SHAPES OF THE AXYSIMMETRIC MEMBRANE NECK

We now go beyond the minimal model described in the previous section by solving the complete Helfrich equation, where the shape of the neck is obtained as part of the solution. To this end, we describe the equilibrium shape of an axisymmetric and mirror symmetric membrane neck connecting two membrane sheets, corresponding to the local geometry of the neck connecting the forespore engulfing and mother cell membranes (see Figs. 1a and c). The energy functional $\tilde{\mathscr{F}}$ consists of a term accounting for membrane bending and tension, $\tilde{\mathscr{F}}_m$, another term accounting for the osmotic pressure pressure difference between cytoplasm and periplasm, $\tilde{\mathscr{F}}_p$, and a term representing any pulling force f on the forespore,

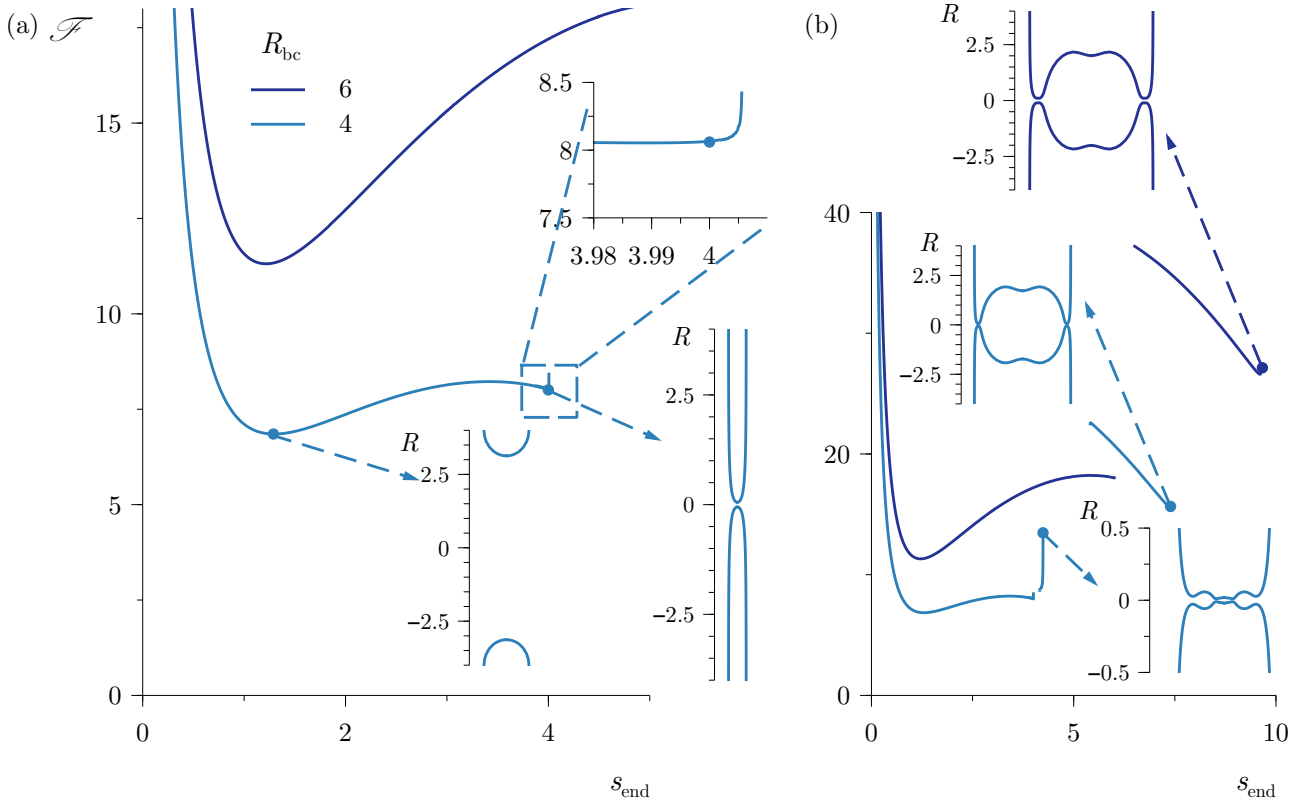

Figure 3. (a) Dimensionless free energy from Eq. (6) as a function of the arc length $s_{\rm end}$ for different values of the radial boundary size $R_{\rm bc}$. The insets show shapes of the neck for $R_{\rm bc} = 4$ and two different values of $s_{\rm end}$, corresponding to two local minima. The zoomed region depicts the sudden increase of free energy as the neck narrows. (b) Same as in panel (a) but displaying some of the multiple branches arising for sufficiently large values of $s_{\rm end}$.

$\tilde{\mathscr{F}}_{\rm f}$ [2–8, 11, 12]:

$$\tilde{\mathscr{F}} = \tilde{\mathscr{F}}_{\rm m} + \tilde{\mathscr{F}}_{\rm p} + \tilde{\mathscr{F}}_{\rm f} = \int_A {\rm d}A \left[\frac{\kappa}{2}(2\tilde{H})^2 + \sigma\right] + \int_V {\rm d}V \Delta\tilde{p} - \tilde{f}L, \tag{6}$$

where $\Delta\tilde{p} = p_{\rm cyto} - p_{\rm peri}$, A is the area of the membrane neck, and V is the volume inside the neck.

For axisymmetric surfaces, it proves convenient to describe the surface in terms of the angle $\theta(s)$ between the contour and the ordinate axis, as parametrized by the arclength s (see sketch in Fig. 1c). To non-dimensionalize Eq. (6), we again introduce the natural length scale $R_{\rm c} = \sqrt{\kappa/(2\gamma)}$ as the characteristic length. The definition of the radial $R(s)$ and axial $Z(s)$ coordinates, and the first variation of Eq. (6) yield the following nonlinear boundary-value problem [11, 13, 14]

$$R' = \cos\theta, \tag{7a}$$

$$Z' = -\sin\theta, \tag{7b}$$

$$\theta'' = -\frac{1}{2}(\theta')^2\tan\theta - \frac{\cos\theta}{R}\theta' + \frac{\cos^2\theta + 1}{2R^2}\tan\theta + \frac{1}{2}\tan\theta + \frac{\Delta p R}{4\cos\theta} - \frac{f}{R\cos\theta}, \tag{7c}$$

where derivatives are with respect to contour length s, $\Delta p = \Delta\tilde{p}R_{\rm c}/\gamma$, and $f = \tilde{f}/(4\pi\gamma R_{\rm c})$. Concerning the boundary conditions, we impose $R(s = s_{\rm end}) = R_{\rm bc}$, $Z(s = s_{\rm end}) = 0$, $\theta(s = s_{\rm end}) = 0$, and $\theta(s = 0) = \pi/2$. The above system of differential equations (7a)–(7c) is solved using the Matlab® built-in boundary-value problem solver `bvp4c` [15, 16].

Fig. 3 shows the dimensionless version of the free energy from Eq. (6), as a function of the arc length $s_{\rm end}$ for different values of the radial boundary size $R_{\rm bc}$ indicated in the legend. When $R_{\rm bc} \gtrsim 3$, the free energy exhibits two local minima. One of them corresponds to a relatively small value of $s_{\rm end}$, where the minimum neck radius is too large, i.e. the neck opens up. The other local minimum occurs at a larger value of $s_{\rm end}$ with a larger associated free energy, corresponding to a narrow neck. Increasing the value of $s_{\rm end}$ beyond the latter local minimum increases the total free energy drastically due to a sharp increase of the bending energy, which prevents membrane fission, as shown for $R_{\rm bc} = 4$ (zoomed region in Fig. 3). When $R_{\rm bc} \lesssim 3$, the free energy only displays one local minimum, which corresponds to that of a narrow neck.

Additionally, Fig. 4 shows the role of the pulling force f and the osmotic pressure difference Δp on the free energy and the shape of the membrane neck. Panel (a) depicts the dimensionless free energy $\mathscr{F}$ as a function of $s_{\rm end}$ with a zero and a non-zero value of f, i.e. $f = 1.5$ (see Table I), and $\Delta p = 0$.

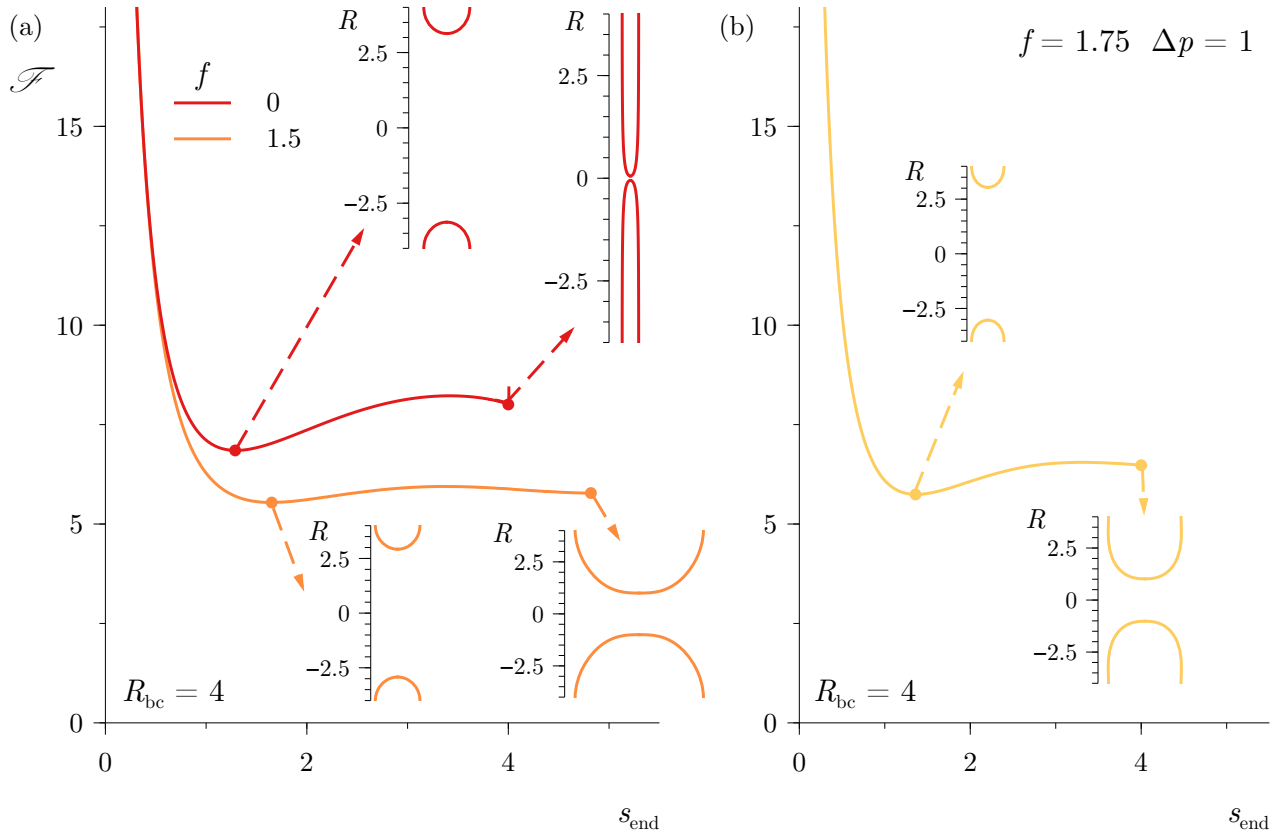

Figure 4. Dimensionless free energy from Eq. (6) as a function of the arc length s_{end} for $R_{bc} = 4$. Panel (a) shows two different values of the dimensionless pulling force f and $\Delta p = 0$, and panel (b) shows a case where $f = 1.75$ and $\Delta p = 1$. The insets show the shapes of the neck for different values of s_{end} indicated with dots.

Table I. Estimates of the physical and dimensionless parameters

Parameter	Value
κ	$20k_BT$ [8]
γ	0.1–10 pN nm^{-1} [17–19]
L	40 nm
$\Delta\tilde{p}$	60 kPa [20]
$\tilde{f}$	50-100 pN [21, 22]
$R_c = \sqrt{\kappa/(2\gamma)}$	2–20 nm
L/R_c	9–90
$\Delta p = \Delta\tilde{p}R_c/\gamma$	0.012–12
$f = \tilde{f}/(4\pi\gamma R_c)$	0.4–4

The insets, showing the shape of the axisymmetric membrane neck at different values of s_{end}, demonstrate that, for the same values of R_{bc} and s_{end}, the pulling force tends to increase both the length of the neck and the minimum neck radius. Panel (b) displays the free energy with a non-zero value of the pulling force and the osmotic pressure difference, i.e. $f = 1.75$ and $\Delta p = 1$. As expected, if we compare this result with that of panel (a) where $\Delta p = 0$, the osmotic pressure difference favors the narrowing of the neck.

We now estimate some of the physical and dimensionless parameters used in the model to determine whether membrane tension and the osmotic pressure difference are able to reduce the neck radius, so that FisB proteins can interact and accumulate in the neck. This estimates are shown in Table I. In particular, we consider a pulling force of $\tilde{f} \sim 50 - 100$ pN, which corresponds to the SpoIIIE stall maximal force [21, 22], and an osmotic pressure difference of $\Delta\tilde{p} \sim 60$ kPa, as estimated in Ref. [20]. We assume that FisB can interact when the radius of the membrane neck is below ~ 10 nm [1], which is within therange of the characteristic neck radius shown in Table I, $R_c = \sqrt{\kappa/(2\gamma)} \sim 2 - 20$ nm, using $\kappa \sim 20k_BT$ [8], and $\gamma \sim 0.1 - 10$ pN nm^{-1} [17–19] (see last section of this Appendix for an upper estimate of the mem-brane tension). According to the model, when $\Delta p = f = 0$, the local minimum of $\mathscr{F}$ corresponding to the larger value of s_{end}, shown in the inset of Fig. 4(a), the dimensional mini-mum radius of the neck is $\tilde{R}_{min} \sim 0.1 - 1$ nm, which is signifi-cantly below the minimum radius required for FisB to interact. Moreover, the local free-energy minimum corresponding to a wider neck yields a minimum neck radius $\tilde{R}_{min} \sim 6.2 - 62$ nm, implying that, if membrane tension increases sufficiently, the neck radius can also be narrow enough for FisB to interact and accumulate inside the neck.

When $f = 1.5$ and $\Delta p = 0$, which corresponds to a range of $\gamma = 0.2 - 0.7$ pN nm^{-1} given that $\tilde{f} \sim 50 - 100$ pN, $\tilde{R}_{\min} \sim 7.8 - 15.6$ nm, corresponding to the membrane neck shown in the right bottom inset of Fig. 4(a). Hence, if we compare the range of the minimum neck radius with that of a null pulling force, it is evident that the radius of the neck increases due to the action of the pulling force. Nonetheless, as we point out above, if membrane tension is large enough, which corresponds to $\tilde{R}_{\min} \sim 7.8$ nm and $\gamma \sim 0.7$ pN nm^{-1} in the previous range of values, the minimum neck radius is small enough for FisB to interact. When $f = 1.75$ and $\Delta p = 1$, which corresponds to $\gamma \sim 0.53$ pN nm^{-1}, $\Delta\tilde{p} \sim 60$ kPa, and $\tilde{f} \sim 100$ pN, $\tilde{R}_{\min} \sim 8.8$ nm, i.e. the estimated value of the osmotic pressure difference only reduces slightly the minimum neck radius, as we also observe in our highly simplified model in Fig. 2(b), thereby favouring the accumulation of FisB in the neck.

FLUX OF LIPIDS

To estimate the membrane tension difference between the two ends of the neck that would drive a flux of lipids from the mother cell to the forespore of $\sim 10^3$ lipids s^{-1} (see *Forespore inflation accompanies membrane fission* in the main text), we balance the force due to the membrane tension difference $\Delta\gamma$ and the drag force on a cylinder (i.e. the neck in our highly simplified model), translating parallel to its axis in an outer bath of viscosity μ,

$$2\pi R\Delta\gamma = \frac{4\pi\mu UL}{\ln(L/R) - 1/2}. \tag{8}$$

Considering that 1 lipid occupies ~ 1 nm^2 and assuming a neck radius of $R \sim 5$ nm, the required lipid velocity along the neck is $U \sim 32$ nm s^{-1}. Taking $L \sim 40$ nm and $\mu \sim 10^{-3}$ Pa s, the estimated membrane tension difference is $\Delta\gamma \sim 3 \times 10^{-7}$ pN nm^{-1}. Hence, a flux of ~ 1000 lipids s^{-1} would require a relatively tiny excess membrane tension in the forespore engulfing membrane compared to the mother cell membrane. So a flux of lipids in the neck could readily provide $\sim$1000 lipids s^{-1} to the forespore membranes.

COMPARING THE STALL FORCE OF SPOIIIE TO THE OSMOTIC PRESSURE DIFFERENCE

Here we analyze how the osmotic pressure difference between the mother cell and the forespore compares to the stall/disassembly force of SpoIIIE [21, 22]. According to Ref. [20], the excess pressure in the forespore is of the order of 60 kPa, which can be related to a salt concentration difference $\Delta\rho$ between the mother cell and the forespore via $\Delta P = N_A k_B T\,\Delta\rho$, yielding $\Delta\rho \sim 25$ mM. Taking the salt concentration in the mother cell to be $\rho_{mc} \sim 200$ mM, the salt concentration inside the forespore is $\rho_{fs} \sim 225$ mM. We can now estimate the energy required to move one salt ion into the forespore as $E = k_B T \log(\rho_{fs}/\rho_{mc}) \sim 2.23 k_B T$. This estimate is of the same order as the energy available from SpoIIIE, which is its stall maximal force, ~ 50 pN [21, 22], multiplied by half the base spacing, i.e. ~ 0.17 nm, since each translocated base of DNA brings $\sim$2 counterions, which yields $E_{\text{SpoIIIE}} \sim 2.1 k_B T$. This near equality of energies suggests that SpoIIIE work near its stall force, by creating the highest pressure difference it can in the forespore.

Additionally we can estimate the membrane tension required to balance this osmotic pressure difference. To this end we assume that the forespore is a sphere surrounded by two membranes, thus the equilibrium excess pressure is given by the Laplace law, $\Delta P = 4\gamma/R_{fs}$. Taking $R_{fs} \sim 400$ nm, $\gamma \sim 6$ pN nm^{-1}, which is slightly below the rupture tension, $\gamma_{rup} \sim 20$ pN nm^{-1} [17–19].

[1] A. Landajuela, M. Braun, C. D. A. Rodrigues, A. Martínez-Calvo, T. Doan, F. Horenkamp, A. Andronicos, V. Shteyn, N. D. Williams, C. Lin, N. S. Wingreen, D. Z. Rudner, and E. Karatekin, PLOS Biology **19**, 1 (2021).
[2] W. Helfrich, Z. Naturforsch. C. **28**, 693 (1973).
[3] P. B. Canham, J. Theor. Bio. **26**, 61 (1970).
[4] O. Y. Zhong-Can and W. Helfrich, Phys. Rev. Lett. **59**, 2486 (1987).
[5] O.-Y. Zhong-Can and W. Helfrich, Phys. Rev. A **39**, 5280 (1989).
[6] U. Seifert and S. A. Langer, EPL **23**, 71 (1993).
[7] U. Seifert, Adv. Phys. **46**, 13 (1997).
[8] T. R. Powers, Rev. Mod. Phys. **82**, 1607 (2010).
[9] A. Karlsson, R. Karlsson, M. Karlsson, A. S. Cans, A. Strömberg, F. Ryttsén, and O. Orwar, Nature **409**, 150 (2001).
[10] P. Dommersnes, O. Orwar, F. Brochard-Wyart, and J. F. Joanny, EPL **70**, 271 (2005).
[11] I. Derényi, F. Jülicher, and J. Prost, Phys. Rev. Lett. **88**, 238101 (2002).
[12] T. R. Powers, G. Huber, and R. E. Goldstein, Phys. Rev. E. **65**, 041901 (2002).
[13] F. Jülicher and U. Seifert, Phys. Rev. E **49**, 4728 (1994).
[14] J. E. Hassinger, G. Oster, D. G. Drubin, and P. Rangamani, Proc. Nat. Acad. Sci. U.S.A **114**, E1118 (2017).
[15] J. Kierzenka and L. F. Shampine, ACM Trans. Math. Softw. **27**, 299 (2001).
[16] L. F. Shampine, J. Kierzenka, M. W. Reichelt, *et al.*, Tutorial notes **2000**, 1 (2000).
[17] D. Needham and R. S. Nunn, Biophys. J. **58**, 997 (1990).
[18] E. Evans, V. Heinrich, F. Ludwig, and W. Rawicz, Biophys. J. **85**, 2342 (2003).
[19] N. Ojkic, J. López-Garrido, K. Pogliano, and R. G. Endres, PLoS Comput. Biol. **10**, e1003912 (2014).
[20] J. Lopez-Garrido, N. Ojkic, K. Khanna, F. R. Wagner, E. Villa, R. G. Endres, and K. Pogliano, Cell **172**, 758 (2018).
[21] J.-F. Allemand and B. Maier, FEMS Microbiol. Rev. **33**, 593 (2009).
[22] N. Liu, G. Chistol, Y. Cui, and C. Bustamante, eLife **7**, e32354 (2018).